Hindawi
International Journal of Energy Research
Volume 2024, Article ID 5772264, 21 pages
https://doi.org/10.1155/2024/5772264

Research Article

Full-Scale Pore and Microfracture Characterization of Deep Coal Reservoirs: A Case Study of the Benxi Formation Coal in the Daning–Jixian Block, China

Tao Wang,[1,2] Guoxiao Zhou,[3] Liyong Fan,[3,4] Daofeng Zhang,[3] Mingli Shao,[5] Rong Ding,[6] Yongzhou Li,[6] Haiyan Hu,[7] and Ze Deng[2]

[1]*School of Geosciences, Yangtze University, Wuhan 430100, China*
[2]*PetroChina Research Institute of Petroleum Exploration & Development, Beijing 100083, China*
[3]*Research Institute of Exploration and Development, PetroChina Changqing Oilfield Company, Xi'an 710018, China*
[4]*National Engineering Laboratory of Low-Permeability Oil & Gas Exploration and Development, Xi'an 710018, China*
[5]*Research Institute of Exploration and Development, Jilin Oilfield Company, Songyuan 131200, China*
[6]*Exploration and Development Division of PetroChina Coalbed Methane Company, Ltd., Beijing 100083, China*
[7]*School of Resource and Environment, Yangtze University, Wuhan 430100, China*

Correspondence should be addressed to Haiyan Hu; 1064069334@qq.com and Ze Deng; dengze@petrochina.com.cn

Received 14 November 2023; Revised 21 March 2024; Accepted 25 March 2024; Published 23 April 2024

Academic Editor: Abdurrahman Saydut

The pore-fracture structure of deep coal reservoirs is highly important for evaluating, exploring, and developing coalbed methane (CBM) resources. This study considers three coal samples from the DJ57 well in the Benxi Formation in the Daning–Jixian block on the eastern margin of the Ordos Basin as the research object. Based on the coal quality parameters of the coal samples, field emission scanning electron microscopy (FE-SEM), gas adsorption experiments, high-pressure mercury intrusion porosimetry (MIP), and microcomputed tomography (micro-CT) scanning were used to quantitatively characterize the nanoscale pores and microscale fractures in deep coal reservoirs and to evaluate the pore-fracture structure at different scales. The results reveal that the pore types in the Benxi Formation coal samples are diverse and include mainly organic matter (OM) pores, inorganic pores (intraparticle and interparticle pores), and microfractures. The organic pores are diverse in shape and mainly exhibit round, oval, and wedge shapes, while the microfractures exhibit slender stripes or serrated curves. The multiscale quantitative characterization of deep coal reservoir pores and fractures is based on a variety of pore characterization methods, and the pore and fracture volume distributions are mainly U-shaped, revealing the coexistence of micropores and microfractures. The volumes of micropores (0.3–2 nm), mesopores (2–50 nm), macropores (50 nm to 10 μm), and microfractures (>10 μm) account for 78.00%, 6.78%, 2.08%, and 13.14%, respectively, of the total pore volume (PV). Based on a full-scale pore-fracture splicing calculation, the total permeability of the Benxi Formation coal samples ranges from 5.77 to 28.22 mD. The observation results indicate that the microfractures are connected to each other, forming a network structure with strong connectivity. The microfractures are mainly associated with pore diameters > 100 μm, accounting for approximately 95% of the total permeability. Moreover, micropores in deep coal reservoirs provide a large space for CBM adsorption, and microfractures enhance the seepage capacity of CBM.

1. Introduction

In recent years, China's CBM exploration and development efforts have focused mainly on shallow and medium layers (depth < 1500 m). As exploration and development continue to progress, increasingly fewer blocks can be developed in a cost-effective manner, and deep CBM will become an important successor field for China's next step in the exploration and development of CBM [1, 2]. China's deep CBM resources are abundant. According to the latest round of

CBM resource evaluation by the Ministry of Land and Resources, the CBM resources 1000–2000 m deep (medium-depth layer) are 18.72×10^{12} m^3, and it is estimated that the national CBM resources deeper than 2000 m (deep layer) are approximately 40×10^{12} m^3, of which the resources at depths of 2000–3000 m are $18 - 20 \times 10^{12}$ m^3 [3, 4]. With the strong investment of state and major oil and gas companies, the exploration and development of deep CBM in recent years have been effective, and the emergence of local high-yield wells on the eastern edge of the Ordos Basin, the southern part of the Qingshui Basin, the eastern part of the Junggar Basin, etc., indicates that China's deep CBM has great potential for development [1, 3].

The pore size distribution (PSD) of coal varies greatly, and the pore characteristics of different sizes and their contributions to CBM adsorption, desorption, diffusion, and migration also differ [5–7]. Investigators mainly classify pore size according to gas occurrence state and divide the pores in coal into micropores (0.3–2 nm), mesopores (2–50 nm), macropores (50 nm to 10 μm), and microfractures (>10 μm) [8–11]. CBM mainly exists in the adsorbed state on pore surfaces and in multiscale (nano-, micro-, and millimetre scales) and multiform connected pore and fissure systems, which act as gas migration and transmission channels. The gases are continuously produced through three stages—desorption, diffusion, and seepage—and diffusion and seepage in nanopores are the initial stages of gas desorption and migration [12, 13]. In CBM development, more attention has been given to the impact of the microfracture scale and connectivity on reservoir permeability, but the development characteristics and connectivity of nanoscale pores may constrain and potentially impact gas desorption and migration [13].

Previous studies on coal pore structure have been carried out in many ways and can be divided into three categories according to experimental principles: fluid injection methods, image analysis methods, and nonfluid injection methods [14, 15]. Fluid intrusion methods mainly include low-pressure CO_2 adsorption (LP-CO_2GA), low-temperature N_2 adsorption (LT-N_2GA), and high-pressure MIP methods [16–20]. Image analysis methods mainly include scanning electron microscopy (SEM), atomic force microscopy (AFM), and transmission electron microscopy (TEM) [19, 21, 22]. Nonfluid injection methods mainly include computed tomography (CT), nuclear magnetic resonance (NMR), small-angle X-ray scattering (SAXS), and small-angle neutron scattering (SANS) [18, 23–26]. Currently, the study of the pore-fracture structure of coal and shale is mainly based on the combination of high-pressure MIP, LT-N_2GA, and LP-CO_2GA methods [16, 18, 19]. A study based on this approach revealed that the pore diameter of marine shales in the Sichuan Basin is generally 10-50 nm and that the pore diameter of transitional shales in the eastern margin of the Ordos Basin is generally 10-20 nm, indicating that the PV of marine and transitional shales is mainly provided by mesopores [27–29]. The pore diameters of coal samples from the Shanxi Formation and Taiyuan Formation are mainly 0.3-1.5 nm, indicating that the PV of these coal samples is mainly provided by micropores [13, 15]. However, the influence of macropores and microfractures in coal reservoirs has not been sufficiently emphasized, resulting in uncertainty in our understanding of the contribution of macropores and microfractures to the reservoir capacity of coal reservoirs. In addition, in high-pressure MIP experiments, due to the compressibility of coal samples, an increase in mercury intrusion pressure leads to compressive deformation of the coal matrix and pore damage, reducing the accuracy of the test results.

Since 2019, deep CBM exploration in the Daning–Jixian block has advanced to a depth of more than 2000 m, and the Jishen 6-7-P-01 well has obtained a high production industrial gas flow of 10.1×10^4 m^3 per day [2, 3]. In 2021, the known reserves of the Daning–Jixian block were 1121.62×10^8 m^3, making it the first large CBM field in China with high abundance below a depth of 2000 m and with reserves exceeding 1000×10^8 m^3, indicating that deep CBM in the Daning–Jixian block has promising development potential [1]. LP-CO_2GA, LT-N_2GA, high-pressure MIP, and micro-CT data tests were carried out on three coal samples from the DJ57 Jingbenxi Formation in the Daning–Jixian block on the eastern margin of the Ordos Basin to identify and quantitatively characterize the pores and fractures of coal reservoirs in the Daning–Jixian block. Additionally, physical experiments on the helium porosity and permeability of the samples were carried out, and the experimental results were compared with numerical results and analysed to determine the influence of microscopic pores and fissures on the occurrence and seepage of CBM in deep coal reservoirs to provide a reference for the exploration and development of deep CBM in the eastern margin of the Ordos Basin.

2. Geological Setting

The Ordos Basin is a typical cratonic marginal superimposed basin in the western part of the North China Plate. The basic tectonic framework was formed in the Yanshanian period and developed in the Himalayan period. Overall, the Ordos Basin features a large syncline with a gentle and long east wing, a steep and short west wing, and upturned north and south wings [30]. According to its underlying properties, structural morphology, and geological evolution history, the Ordos Basin is divided into six first-order tectonic units, namely, the Yimeng Uplift, West Margin thrust belt, Weibei Uplift, Tianhuan Depression, Jinxi fault belt, and Yishan slope (Figure 1(a)) [30]. The research area is located in the Daning–Jixian area on the eastern margin of the Ordos Basin. The Daning–Jixian block is located at the southern end of the Jinxi fault belt and the southeastern margin of the Yishan slope on the eastern margin of the Ordos Basin, and its southern neighbour is the Yanchuan block.

The coal-bearing strata in the study area are mainly in the upper Palaeozoic Carboniferous system and Permian system, and the corresponding sedimentary environment changes from marine to continental facies; these strata can be divided into the Shanxi Formation, Taiyuan Formation, and Benxi Formation. The Shanxi Formation is dominated by delta facies, while the Taiyuan Formation and Benxi Formation contain delta, lagoon, tidal flat, and shallow shelf deposits from north to south. In the vertical direction,

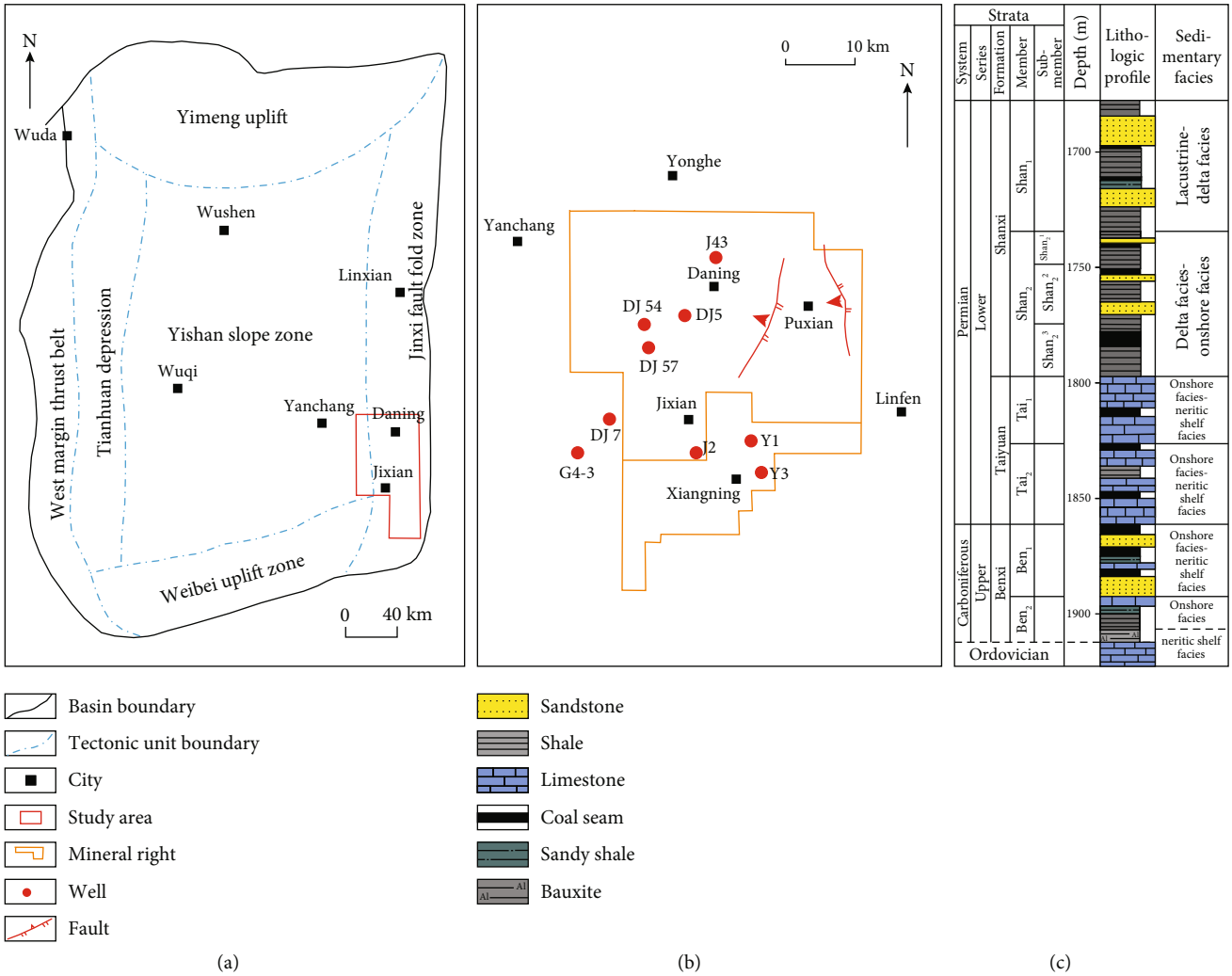

Figure 1: Location and stratigraphic column of the study area. (a) Study area location; (b) well location in the study area; (c) stratigraphic profile of the study area.

mudstone is alternately distributed with coal and sandstone, and pure mudstone rarely develops [30, 31]. The main target layers are the Shanxi Formation coal seam, Taiyuan Formation coal seam, and Benxi Formation coal seam [31]. The thickness of the Shanxi Formation coal seam is only 1–3 m, the thickness of the Taiyuan Formation coal seam is approximately 1–6 m, and the thickness of the Benxi Formation coal seam is greater, ranging from 5 to 12 m; these seams are the main coal seams in the Ordos Basin. The no. 8 coal seam of the Benxi Formation has a wide and continuous distribution and large thickness; among these seams, the plane spreading area between 2000 and 3500 m is approximately 6.9×10^3 m^2, which is the most favourable deep CBM exploration target of the Benxi Formation (Figures 1(b) and 1(c)) [31].

3. Samples and Methods

3.1. Sample Selection. Three fresh coal samples from newly drilled wells in the Daning–Jixian area in the eastern margin of the Ordos Basin were selected; all of these samples were obtained from the upper, middle, and lower parts of the Benxi Formation at the DJ57 well. To eliminate the influence of the heterogeneity on the experimental data, before the experiment, the core was cut by wire cutting equipment, and a cylindrical coal sample (50 mm high with a diameter of 25 mm) was cut for micro-CT scanning, helium porosity, and permeability measurements. Then, the cylindrical coal sample was cut and crushed. The resulting pieces were subjected to vitrinite reflectance (R_o) and maceral analysis, proximate analysis, FE-SEM, high-pressure MIP, LT-N_2GA, and LP-CO_2GA experiments (Figure 2). R_o measurements (80 points) and maceral analysis (500 points) were performed randomly in oil-immersed reflected light according to the Chinese standards GB/T 6948–2008 and SY/T 6414–2014, respectively. The moisture content (M_{ad}), ash yield (A_d), volatile yield (V_{daf}), and fixed carbon (FC_{ad}) content of the coal samples were analysed in accordance with the Chinese standard GB/T 212–2002. Helium porosity and permeability were measured in cylindrical coal samples according to the Chinese standard GB/T 34533–2017. The test results are shown in

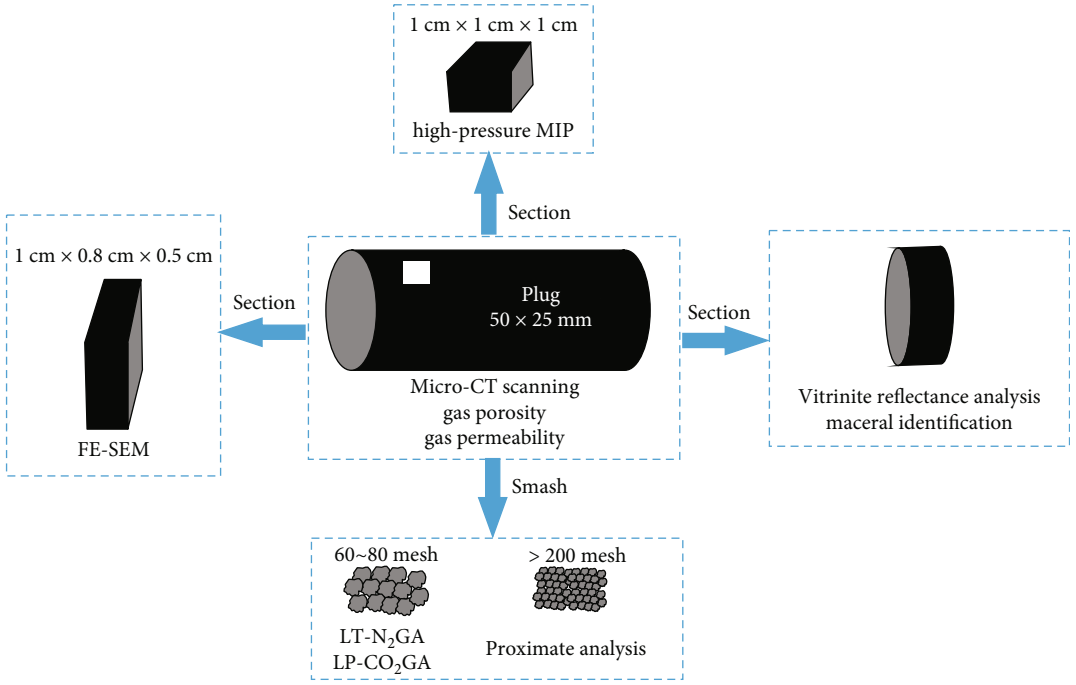

Figure 2: Schematic illustration of the sample preparation methods.

Table 1: Properties of the Benxi Formation coal in the Daning–Jixian block.

Sample ID	Depth (m)	Formation	$R_{o,max}$ (%)	He porosity (%)	Permeability (mD)	Maceral composition (%)				Proximate analysis (%)			
						V	I	E	M	M_{ad}	A_d	V_{daf}	FC_{ad}
DJ57-1	1884.28	Benxi	2.13	6.64	11.01	70.33	13.87	1.93	13.87	0.85	28.65	7.99	62.51
DJ57-2	1886.21	Benxi	2.12	3.23	8.36	79.96	10.5	0	9.54	0.77	29.73	8.98	60.52
DJ57-3	1887.32	Benxi	2.20	6.34	1.42	76.48	4.78	0	18.74	0.86	24.74	8.06	66.34

Notes: $R_{o,max}$ = maximum reflectance of vitrinite; V = vitrinite; I = inertinite; E = exinite; M = mineral; M_{ad} = moisture content; A_d = ash yield; V_{daf} = volatile yield; FC_{ad} = fixed carbon content.

Table 1. The porosity and permeability tests of 3 coal samples from the Benxi Formation in the DJ57 well in the Daning–Jixian block reveal that the coal sample porosity ranges from 3.23% to 6.64% (mean 5.40%), and the permeability ranges from 1.42 to 11.01 mD (mean 6.93 mD).

3.2. Experimental Methods

3.2.1. FE-SEM. The qualitative characterization of coal samples was mainly realized through direct observation and description of pores via FE-SEM [14, 20]. For this, a small rectangular coal sample with dimensions of 10 mm (length) × 8 mm (width) × 5 mm (height) was prepared. Then, a HITACHI IM 4000 argon ion polishing instrument produced by Hitachi company was used to continuously bombard the cross-section of the vertical shale formation under a certain energy under vacuum conditions to obtain a super smooth surface. Argon ion polishing lasted approximately 3 hours. The sample preparation and polishing process can effectively avoid damage to the sample surface during the mechanical polishing process and can restore the true pore shape of the sample. The polished samples were imaged with a Helios NanoLab 660 double-beam scanning electron microscope produced by the FEI company to obtain high-resolution SEM images. Through a series of SEM images with different resolutions, the pore morphology, relationship between pores and particles, pore distribution, pore size, and pore connectivity can be directly observed. The experimental procedure was carried out in accordance with the Chinese Oil and Gas Industry Standard SY/T 5162–2014.

3.2.2. Gas Adsorption. The gas adsorption experiment was carried out by an AutoSorb-iQ-MP-C automatic physical chemical adsorption instrument. The particle size of the sample was 60-80 mesh. Before the analysis of the LT-N_2GA experiment, the samples were degassed at 110°C for 12 hours to remove the water and volatile substances in the samples. Then, the degassed samples were moved to the analysis station, and the adsorption-desorption test was carried out at 77 K with high-purity N_2 as the adsorbent. The structural parameters, including the PV, specific surface area (SSA), and PSD, were obtained by the Brunauer–Emmett–Teller (BET) and nonlocal density functional theory (NLDFT) models [32–35]. The experimental procedure was carried out in strict accordance with GB/T 21650.2–2008. The sample pretreatment of the LP-CO_2GA experiment was

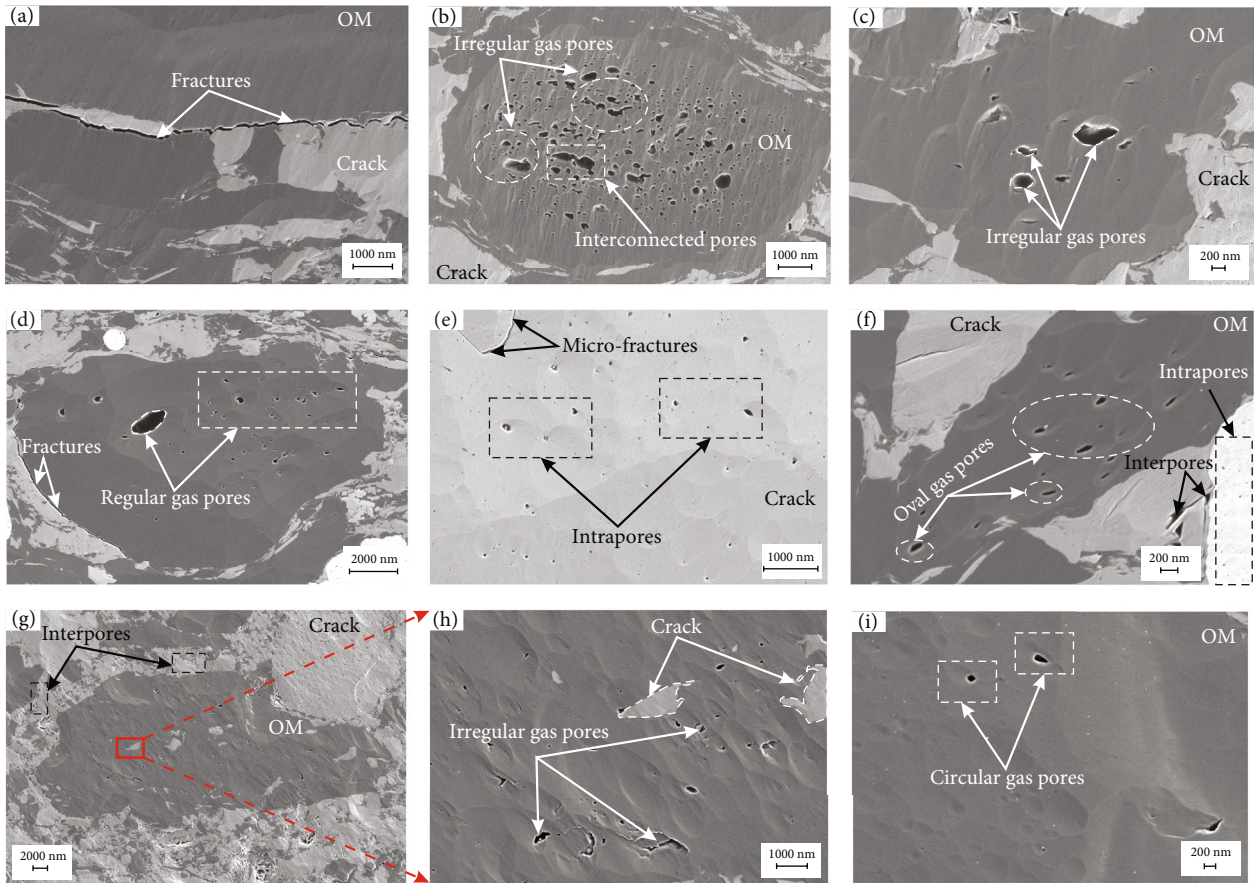

Figure 3: FE-SEM images of the pore structure of the Benxi Formation coals from the deep Daning–Jixian block study area. (a–c) Sample DJ57-1; (d–f) sample DJ57-2; (g–i) sample DJ57-3.

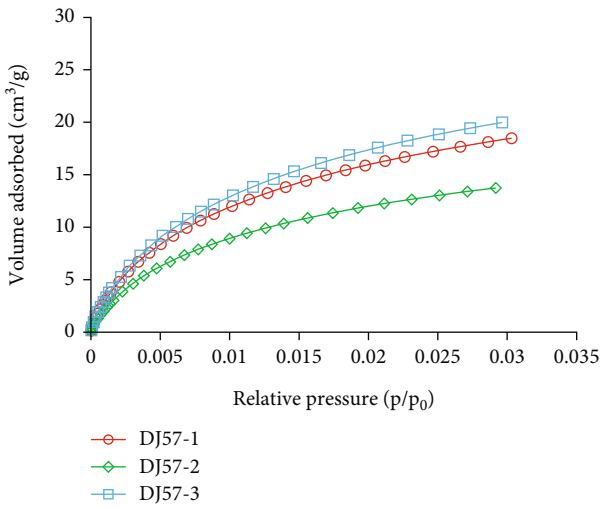

Figure 4: CO_2 adsorption curves.

similar to that of the LT-N_2GA experiment. A total of 1–2 g of 60–80 mesh powder sample was degassed for 16 hours, and the adsorption test was carried out at 273 K with high-purity CO_2 as the adsorbent. The structural parameters, including the PV, SSA, and PSD, were obtained based on the NLDFT theoretical model [36, 37]. The experimental procedure was carried out in accordance with GB/T 21650.3–2011.

3.2.3. High-Pressure MIP. An AutoPore 9505 mercury injection instrument produced by Quantachrome Instruments, U.S., was used for the high-pressure MIP testing. During the test, the mercury injection pressure provided by this instrument reached 413 MPa, and the corresponding test pore diameter limit was approximately 3 nm. For this test, coal was processed into a cube of 1 cm^3, and the surface of the coal sample was smoothed to avoid the "pitting effect." The sample was also continuously dried for 8 hours at 105°C to ensure that the original pores of the coal sample were not destroyed by the high temperature, the impurities and gases inside the sample were effectively eliminated during the test, and the vacuum inside the instrument was maintained. According to the data automatically collected by the instrument during the process of mercury injection and mercury withdrawal, pore structure parameters such as the PV, SSA, and PSD were obtained by the Washburn equation [38]. The experimental process was carried out in accordance with GB/T 21650.1–2008.

3.2.4. Micro-CT Scanning. Micro-CT scanning is a commonly used test method that can quantitatively characterize the spatial distribution and connectivity of some macropores

Table 2: Pore structure parameters of the coal samples.

Sample ID	Depth (m)	Formation	High-pressure MIP		LT-N_2GA			LP-CO_2GA		
			PV (cm^3/g)	SSA (m^2/g)	PV (cm^3/g)	SSA (m^2/g)	DDFT (nm)	PV (cm^3/g)	SSA (m^2/g)	DDFT (nm)
DJ57-1	1884.28	Benxi Fm.	0.014	7.42	0.007	3.96	3.775	0.056	190.36	0.501
DJ57-2	1886.21	Benxi Fm.	0.018	10.09	0.004	2.46	1.22	0.042	143.64	0.501
DJ57-3	1887.32	Benxi Fm.	0.026	16.31	0.005	3.57	4.411	0.061	207.37	0.501

Notes: MIP = mercury intrusion porosimetry; LT-N_2GA = low-temperature N_2 adsorption; I = inertinite; LP-CO_2GA = low-pressure CO_2 adsorption; PV = pore volume; SSA = specific surface area; DDFT = average pore width according to the DFT model.

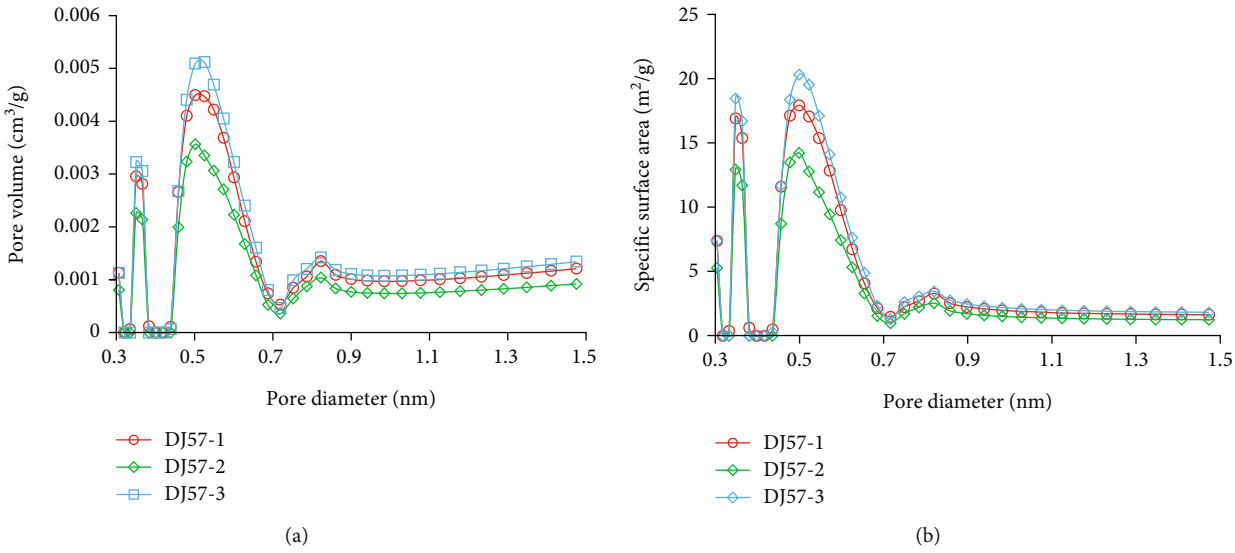

Figure 5: PSD characteristics of the coal samples based on the LP-CO_2A experiment. (a) Pore volume distribution and (b) pore specific surface area distribution.

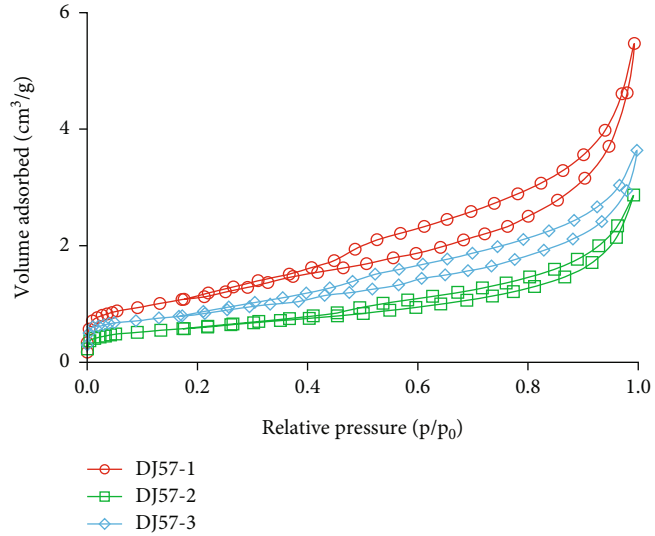

Figure 6: N_2 adsorption-desorption curves.

and microfractures in coal samples [22, 23]. A nanoVoxel3502E multiscale high-resolution X-ray three-dimensional microscopic imaging system produced by Sanying Precision Instruments Co., Ltd., was used to scan the coal samples, with a system resolution of more than 500 nm. Before the micro-CT scanning experiment, a cylindrical coal sample with a

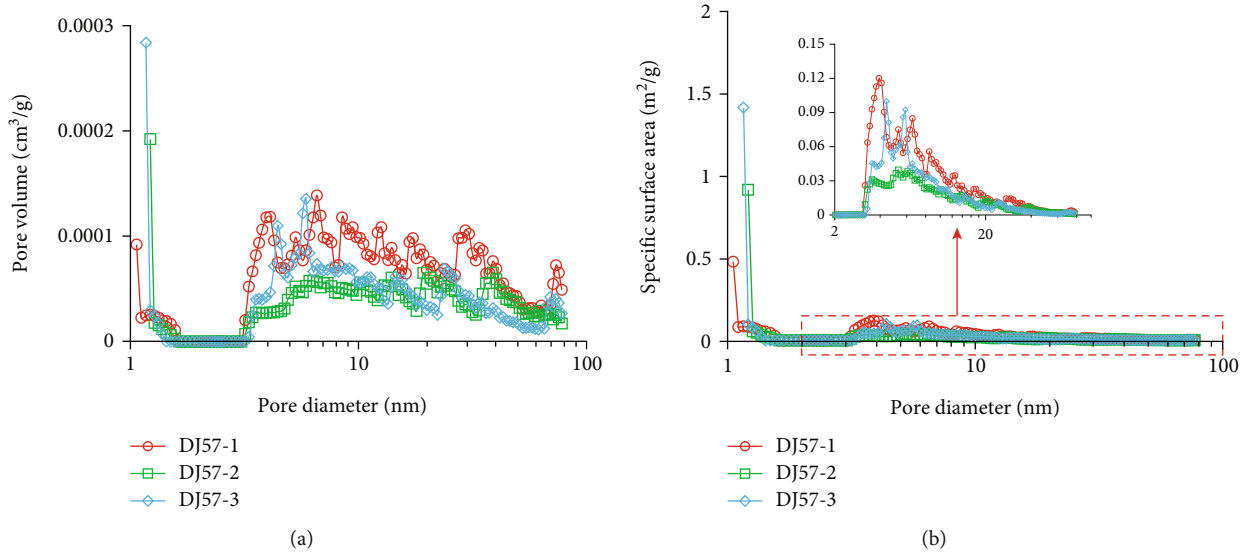

Figure 7: PSD characteristics of the coal samples based on the LT-N_2A experiment. (a) Pore volume distribution and (b) pore specific surface area distribution.

diameter of 25 mm and a length of approximately 5 cm was drilled along the vertical direction. After the cylindrical coal sample was fixed, it was placed vertically in the micro-CT scanning device. The X-ray source position was adjusted, and the sample was prepared for micro-CT scanning. The micro-CT scanning voltage was 60 kV, and the experimental temperature was 25°C. Due to the influence of the cylindrical coal sample thickness and exposure time, the minimum pore size characterized by the micro-CT approach was 10 μm.

4. Results

4.1. Pore-Fracture Morphology Analyses Based on FE-SEM Images. FE-SEM was used to observe and analyse the pore and fracture morphology of the Benxi Formation coal samples from the Daning–Jixian block. There are many nanometre-scale pores and microfractures in the Benxi Formation coal samples. At present, classification schemes for coal reservoir pores have not been unified [14, 20]. In this study, referring to the classification scheme proposed by Loucks et al. [7], the pores in the Benxi Formation coal samples are divided into OM pores, inorganic pores, and microfractures. The microfractures are shrinkage-induced fractures. OM pores are mainly distributed in the coal matrix (Figures 3(b)–3(d), 3(f), 3(h), and 3(i)), with various pore shapes, including regular round shapes and oval shapes (Figures 3(d), 3(f), and 3(i)) and irregular wedge shapes (Figures 3(h) and 3(c)), as well as dispersed and distributed spongy connected pores (Figure 3(b)). Moreover, there are isolated pores (Figures 3(d), 3(f), and 3(i)) with pore diameters ranging from 4.4 to 220 nm, which provide space for CBM and are important pore types for CBM reservoirs. Inorganic pores can be divided into intragranular pores and intergranular pores. The former is generally distributed between clay and mineral particles or between rigid particles (Figures 3(f) and 3(g)) and is mainly related to the preservation of primary pores, which are usually manifested as

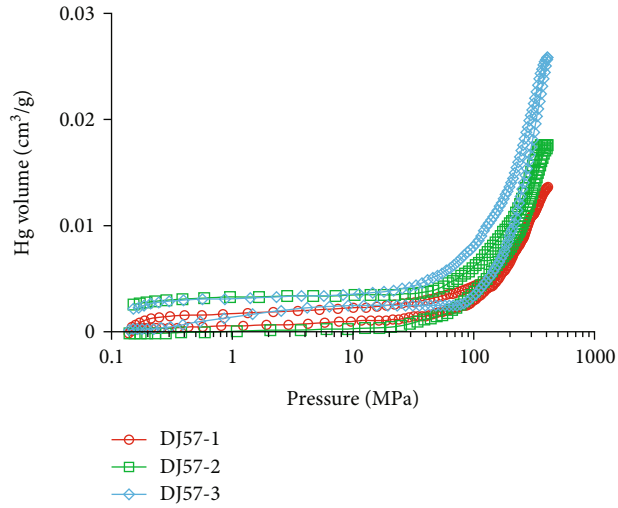

Figure 8: High-pressure mercury intrusion-extrusion curves.

isolated pores with poor connectivity (Figures 3(c), 3(f), and 3(h)). Moreover, their pore diameter is larger, generally greater than 300 nm. The latter component usually develops in dissolved mineral particles and is poorly connected to the external environment (Figures 3(e) and 3(f)), and its pore diameter is generally small, between 20 and 50 nm. Microfractures are well developed in the Benxi Formation coal samples. Most of the microfractures are distributed inside the mineral particles or at the edges of the rigid particles (Figures 3(a), 3(d), and 3(e)). The microfractures are either elongated or zigzag-shaped and have a wide range of sizes. The microfracture lengths are approximately 3~50 μm, and the microfracture widths are approximately 20 nm to 1 μm.

Figure 3 shows the morphology of the pores and microfractures, and it can be concluded that (1) the OM pores are mainly circular, elliptical, and wedge-shaped pores; (2) the inorganic pores are mainly closed pores, and some are open

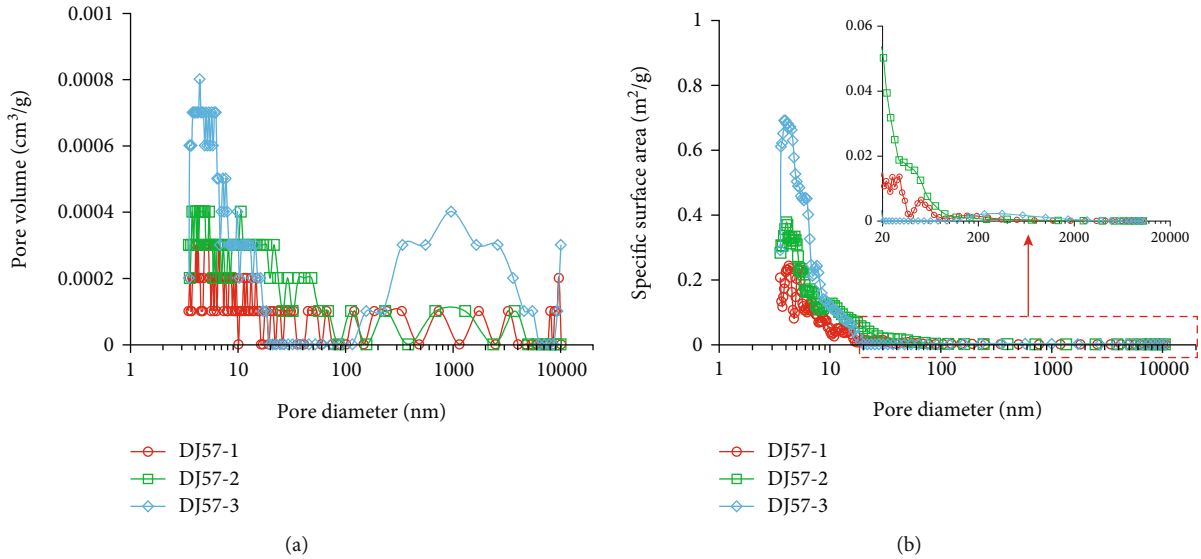

Figure 9: PSD characteristics of the coal samples based on the high-pressure MIP experiment. (a) Pore volume distribution and (b) pore specific surface area distribution.

pores (such as parallel plate pores and conical pores); and (3) the microfractures are mainly elongated or zigzag-shaped. The pore types of the middle-shallow coal seam mainly include initially developed pores, cavity pores, intercrystalline pores, and dissolution pores. The microfractures of the middle-shallow coal seam are relatively developed, and no filling material is found in the microfractures; horizontal bedding fractures are common there, so the permeability of the middle-shallow coal seam is greater than that of the deep coal reservoir.

4.2. Analysis of LP-CO_2GA Data. Figure 4 shows the LP-CO_2GA curves of the coal samples from the study area, which exhibit similar characteristics. The amount of CO_2 adsorbed by these samples steadily increases with increasing pressure. According to the IUPAC classification, these curves are type I isotherms [39]. The adsorption of CO_2 by sample DJ57-3 is the highest, reaching 20.07 cm^3/g, indicating that this sample has more micropores than the other samples. The amount of CO_2 adsorbed by DJ57-2 is the lowest, at only 13.82 cm^3/g, indicating that there are relatively few micropores in the sample. Based on the calculation of the LP-CO_2GA data with the NLDFT model, the PSD curves and pore structure parameters of the coal samples in the pore size range of 0.3–1.5 nm were obtained (Table 2). The SSA of the micropores ranges from 141.64 to 207.37 m^2/g (mean 180.46 m^2/g), which is much greater than the result of the LT-N_2GA analysis. This result shows that the proportion of micropores in coal is high. The volume of the micropores ranges from 0.042 to 0.061 cm^3/g (mean 0.053 cm^3/g). The mean pore diameter of all the samples is 0.501 nm. The distribution characteristics of micropore size based on LP-CO_2GA data show that the micropore development of coal samples generally presents a multimodal peak distribution of 0.3–0.4 nm, 0.4–0.7 nm, and 0.8–0.9 nm (Figure 5). The increase in PV and SSA in the >1.0 nm pore diameter segment slows significantly, and the corresponding PV and SSA are very low. Because the micropores in the coal samples are relatively developed and have a large SSA, they can provide many adsorption sites for gas occurrence [13, 40].

4.3. Analysis of LT-N_2GA Data. Figure 6 shows the N_2 adsorption-desorption curves of the coal samples from the study area. The morphology of the adsorption curves of all the coal samples slightly varies, but the overall shape is a reverse "S." According to the six types of physical adsorption isotherms proposed by the IUPAC, the N_2 adsorption curve is close to the type IV adsorption isotherm [39]. In the low-pressure stage ($p/p_0 < 0.1$), the gas adsorption capacity increases rapidly with increasing relative pressure. In this stage, micropore filling occurs, and single-molecule adsorption is the main adsorption mechanism, indicating that the gas adsorption capacity at this stage is mainly related to micropores and some mesopores [13]. When the relative pressure further increases ($p/p_0 = 0.1$-0.9), the adsorption amount of N_2 increases slowly, indicating that the single-molecular layer adsorption process has ended and that the multimolecular layer adsorption process has begun. When the relative pressure continues to increase to nearly 1.0, the adsorption capacity increases rapidly again, but there is no adsorption when the relative pressure approaches the saturated vapour pressure (p_0), indicating that there is a certain amount of open macropores in the coal samples.

Previous studies have shown that the pore morphology of coal can be further evaluated by the type of N_2 adsorption-desorption curve and the shape of the hysteresis loop [41]. For all the samples, the adsorption and desorption curves do not coincide in the region with higher relative pressure ($p/p_0 > 0.45$), and a hysteresis loop forms. The LT-N_2GA branch of the coal samples from the study area is steep at saturated vapour pressure (p_0), the desorption curve is similar to the adsorption curve but steep at saturated vapour pressure (p_0), and the adsorption and desorption curves tend to coincide, forming a narrow hysteresis loop

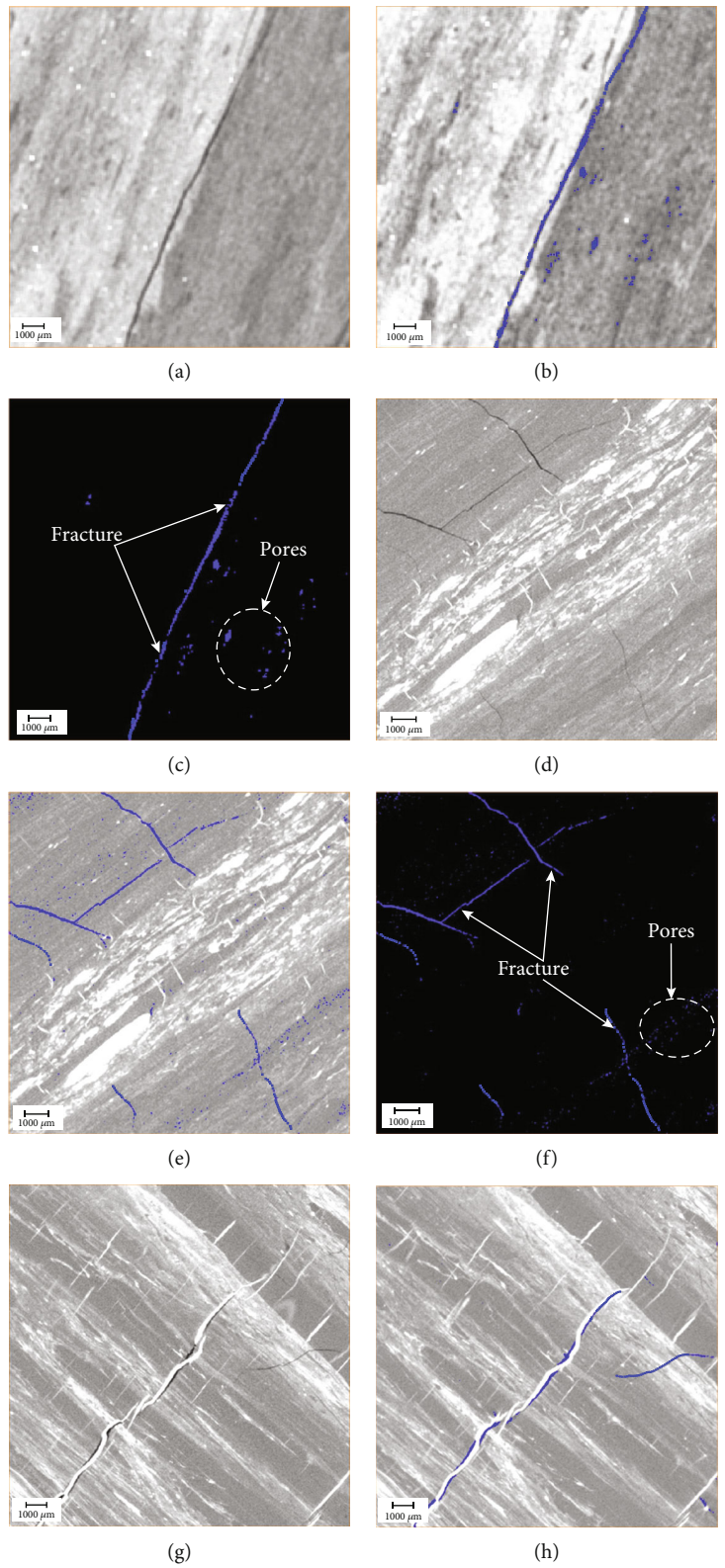

Figure 10: Continued.

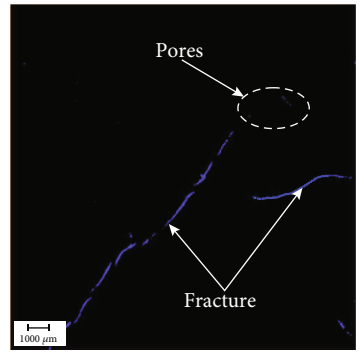

(i)

Figure 10: Two-dimensional distribution of microfractures in the coal analysed via micro-CT. (a, d, g) Original micro-CT images of DJ57-1, DJ57-2, and DJ57-3, respectively; (b, e, and h) corresponding images of the main pore and fractures DJ57-1, DJ57-2, and DJ57-3, respectively; (c, f, i) corresponding images of the final interpretations of DJ57-1, DJ57-2, and DJ57-3, respectively.

between them. This type of curve is similar to the H3 type proposed by the IUPAC and has the characteristics of the H4 type, indicating that the coal samples from the study area contained many nanoscale pores and that the pore types are mainly conical pores, ink bottle pores, and slit pores.

Based on the NLDFT model, LT-N_2GA data were calculated to obtain the PSD curve and pore structure parameters of the coal samples in the pore size range of 1.06–78 nm (Table 2). The DFT PV of the coal samples ranges from 0.004 to 0.007 cm^3/g (mean 0.005 cm^3/g). The DFT SSA ranges from 2.46 to 3.96 m^2/g (mean 3.33 m^2/g). The average pore diameter is 3.135 nm corresponding to a mesopore. The PSDs of the coal samples from the study area are shown in Figure 7. With increasing pore size, the PV of the stage decreases significantly. When the pore size is larger than 10 nm, the change in PV is small, indicating that the proportion of 10 nm pores is low.

4.4. Analysis of High-Pressure MIP Data. Figure 8 shows the intrusion-extrusion curves of coal samples from the study area. The shape of this curve can reflect the distribution characteristics of the pore throat sizes and the quality of the pore connectivity [15]. Overall, the curve shapes are similar, indicating that the coal samples in the study area have relatively similar structures. The high-pressure MIP curve has the characteristics of a gentle front end and a steep back end. When the mercury inlet pressure is less than 100 MPa, the inflow is slow, and the corresponding pore size mainly increases, indicating that the pores are relatively undeveloped. When the pressure reaches approximately 100 MPa, the mercury intake increases rapidly, reflecting the development of many nanoscale pores in the coal sample. The mercury removal efficiency of all the coal samples is high, which reflects that the pores developed in the coal samples are mostly open pores with good connectivity.

Based on the Washburn equation, the pore size distribution and pore structure parameters of the coal samples with pore diameters ranging from 3 nm to 10 μm were obtained by calculating high-pressure MIP experimental data (Table 2). The PV of the coal samples varies from 0.014 to 0.026 cm^3/g (mean 0.019 cm^3/g), and the SSA varies from 7.42 to 16.31 m^2/g (mean 11.27 m^2/g). The PSDs of the coal samples from the study area are shown in Figure 9. The highest mercury intake occurs within the pore size range of less than 30 nm, nearly 80% of the mercury saturation, indicating that the coal samples from the Benxi Formation have mainly nanoscale pores.

4.5. Micro-CT Analysis Data. A micro-CT was used to identify three different components in coal, namely, the pores and fractures, the minerals, and the coal matrix. High-density minerals are shown in white in the corresponding images, low-density pores and fractures are shown in black in the corresponding images, and the coal matrix is shown in grey in the corresponding images (Figure 10) [42–44]. The superposition of the pores and fractures, coal matrix, and minerals constitutes the micro-CT three-dimensional pore-fracture structure model of the coal sample (Figure 11). Figures 10 and 11 show that microfractures are mainly developed in all the coal samples, and microfractures are mainly manifested as isolated points, interconnected slender strips, or zigzag curves. Large-scale microfractures constitute the coal reservoir fracture system, which is the main seepage channel controlling the production of CBM. In addition, there are micron-scale pore systems in all the coal samples, which are distributed in almost every area of the coal sample, mainly in irregular ellipsoid shapes and multilateral shapes, and some in relatively concentrated flake shapes, which are conducive to the diffusion of free gas in the coal reservoirs. The fracture system and micron-scale pore system of the coal reservoir together constitute the complex dual-porosity structure of coal [45–47]. In general, in three-dimensional space, the microfractures are connected to each other, forming a network structure, and the overall connectivity is good (Figure 11). The total volume, microfracture volume, and SSA of the coal samples were determined via micro-CT scanning and three-dimensional reconstruction. The coal density was calculated with the micro-CT data to compare it with the measured density of the coal samples. Finally, the microfracture volume of the coal samples was calculated to be 0.0031–0.0116 cm^3/g. The SSA of the microfractures ranges from 0.0002 to 0.0009 m^2/g, among which DJ57-1 has the largest microfracture volume, and DJ57-2 has the smallest volume. As shown in Figure 11, the relationship between the equivalent pore

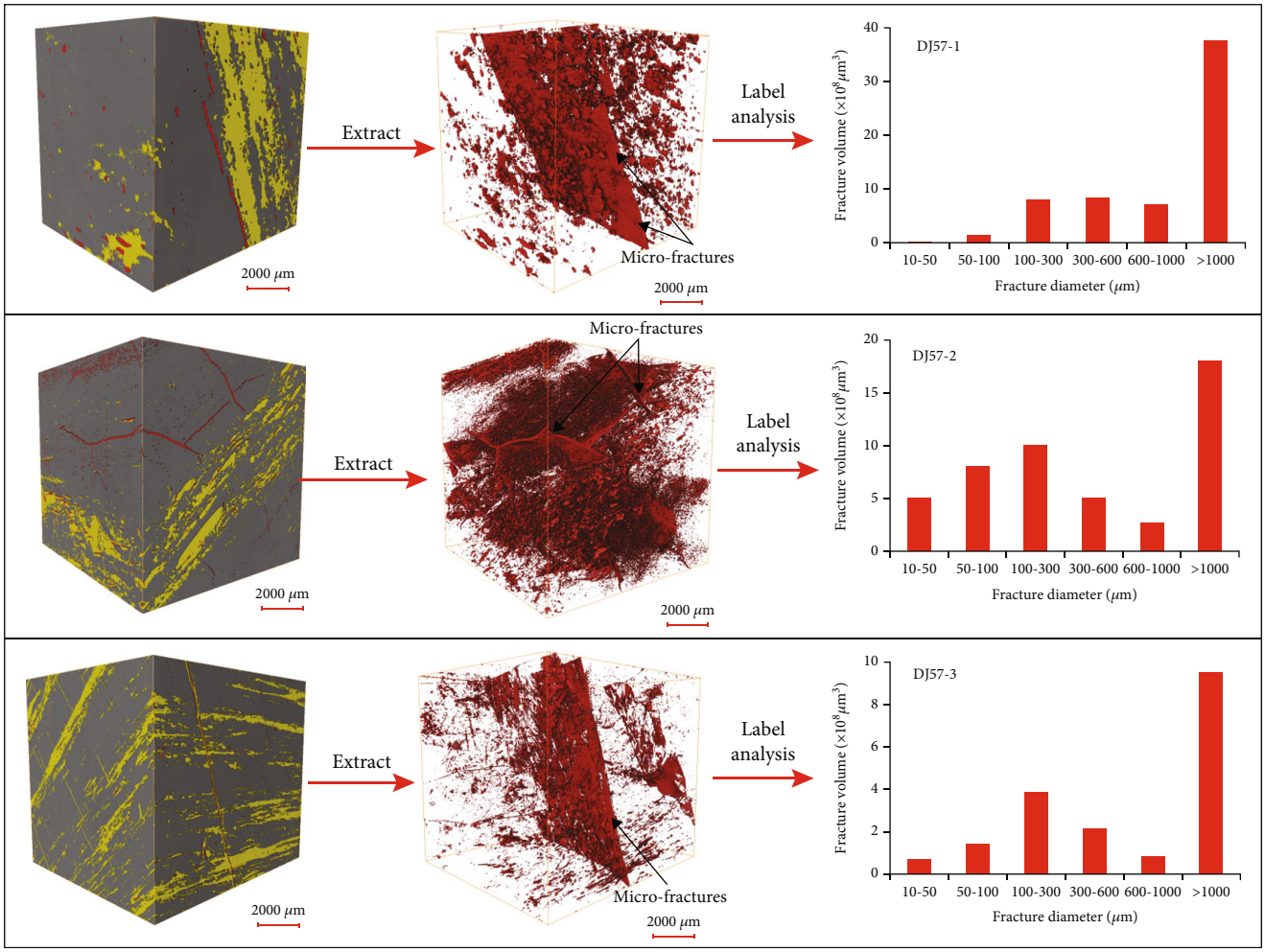

Figure 11: Three-dimensional reconstruction of the Benxi coal sample analysed via micro-CT (black = pores and fractures; grey = matrix; white = minerals).

diameter and volume of micron-scale pores and fractures identified via CT scanning is dominated by fractures > 1000 μm.

5. Discussion

5.1. Full-Scale Pore-Fracture Distribution Characteristics

5.1.1. Principle of Dominant Pore Size Segments. Due to the different pore size ranges measured by different methods, it is difficult to fully characterize pores and fractures by a single method [48–52]. According to the test principle and calculation model, micro-CT scanning, high-pressure MIP, LT-N_2GA, and LP-CO_2GA all have their own advantageous pore size segments, in which the corresponding method can accurately characterize the pore-fracture structure [35, 48, 52]. As shown in Figure 12, rectangles of different widths represent pores and fractures of different scales. According to the analysis of the above test methods, CO_2 is an ideal micropore test probe. At 273 K, the molecular kinetic diameter of CO_2 is only 0.33 nm, and its saturated vapour pressure is relatively high (3480 KPa) [35, 48]. At a higher relative pressure, the micropores can be filled, the diffusion rate is fast, and the pores in the pore size range of 0.3–1.5 nm can be accurately characterized; this is the advantageous pore size segment of the LP-CO_2GA experiment. However, because CO_2 molecules do not undergo capillary condensation in meso- or macropores, the Kelvin equation is no longer applicable, and the traditional Barrett–Joyner–Halenda (BJH) model cannot be used to test meso- or macropores [49–51]. For the LT-N_2GA method, the larger the pore size filled with gas during the test process, the closer the relative pressure (p/p_0) required is to 1. Due to the accuracy of the sensor and control mechanism of the instrument, it is impossible to accurately test macropores with a pore size > 50 nm. For pores with pore sizes < 1.5 nm, N_2 molecules must be filled under very low relative pressure (10^{-7}–10^{-5}). At this time, the N_2 diffusion rate is extremely slow, and adsorption equilibrium can take a long time to reach or even may never be reached. As a result, it is difficult to test pores with pore sizes < 1.5 nm via this method. Therefore, the pore size range of 1.5–50 nm is the dominant pore size segment of the LT-N_2GA experiment. The maximum theoretical pore size of the high-pressure MIP method ranges from 3.6 nm to 10 μm,

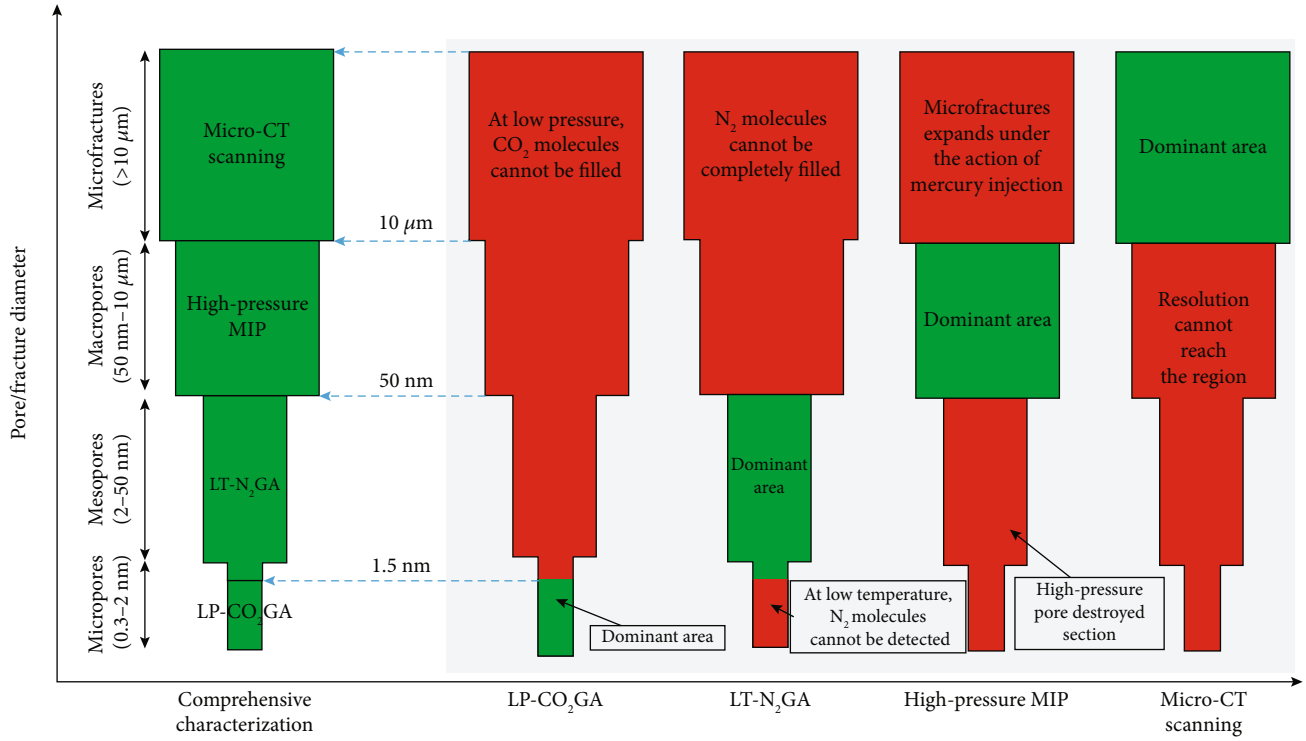

Figure 12: Principle of dominant pore size segments for nitrogen adsorption, mercury injection, and CT experiments.

covering the distribution of mesopores and macropores. However, due to the compressibility of coal, fractures easily expand under the action of high-pressure mercury; on the other hand, when the mercury inlet pressure is greater than 30 MPa (pore diameter of approximately 50 nm), high-pressure mercury destroys micropores [13, 35, 52]. Therefore, high-pressure MIP experiments are not suitable for characterizing mesoporous and large-scale fractures, but they can more accurately characterize macropores ranging in size from 50 nm to 10 μm, which is the dominant aperture segment of high-pressure MIP experiments. The resolution of a micro-CT scan is related to the size of the coal sample. For the cylindrical sample tested in this work (50 mm high with a diameter of 25 mm), the scanning resolution was 10 μm. Although micro-CT scans are limited by their resolution, they can accurately characterize fractures in aperture segments larger than 10 μm, thus compensating for the inability of high-pressure MIP experiments to accurately characterize fractures.

In summary, this study examined the test data for the optimal aperture range of each gas adsorption method and selected a suitable calculation model. The LP-CO_2GA experimental data were calculated based on the NLDFT model, and the effective aperture measurement range is 0.3–1.5 nm. The LT-N_2GA experimental data can be calculated based on the NLDFT model, and the effective aperture measurement range is 1.06–78 nm. The overlap between the two models is 1.06–1.50 nm. Due to the characteristics of the test technology and the calculation model itself, the overlap interval was characterized by the results of the LP-CO_2GA experiment. Based on the Washburn equation, the effective aperture measurement range of 3 nm to 10 μm was calculated. The overlap between the results of this method and the results of the LT-N_2GA experiment is 3.0–50 nm. Due to the matrix compression effect when the pressure in the high-pressure MIP experiment was greater than 30 MPa, the overlap interval was characterized by the results of the LT-N_2GA experiment. The resolution of the micro-CT scans is approximately 10 μm, which is close to the upper limit of the experimental results for high-pressure MIP in this paper. To increase the accuracy and precision of the analysis results, the advantages of certain tests in the corresponding intervals were fully utilized to ensure the continuity of the pore-fracture results in the entire aperture range (Figure 12).

5.1.2. Comprehensive Characteristics of Full-Scale Pores and Fractures. According to the joint characterization results of the pore and fracture volume of the coal samples from the study area (Figure 13), the pore and fracture volume distributions are mainly bimodal, reflecting the coexistence of micropores and microfractures, mainly concentrated in the ranges of 0.3–1.5 nm and >100 μm, respectively. The pore and fracture volumes of the coal samples range from 0.057 to 0.075 cm^3/g (mean 0.067 cm^3/g). Among them, the PVs are mostly associated with the micropores, which provide volumes of 0.042–0.061 cm^3/g (mean 0.053 cm^3/g). The second-most common types of fractures and pores are microfractures and mesopores, with the volume of microfractures ranging from 0.003 to 0.012 cm^3/g and that of mesopores ranging from 0.003 to 0.006 cm^3/g. The macropore PV is the smallest, between 0.001 and 0.002 cm^3/g. The proportions of pore and fracture volumes at different scales are different (Figure 13 and Table 3). Among them, the pore and fracture volumes in the coal samples are dominated by micropores, with an average proportion of 78.00%,

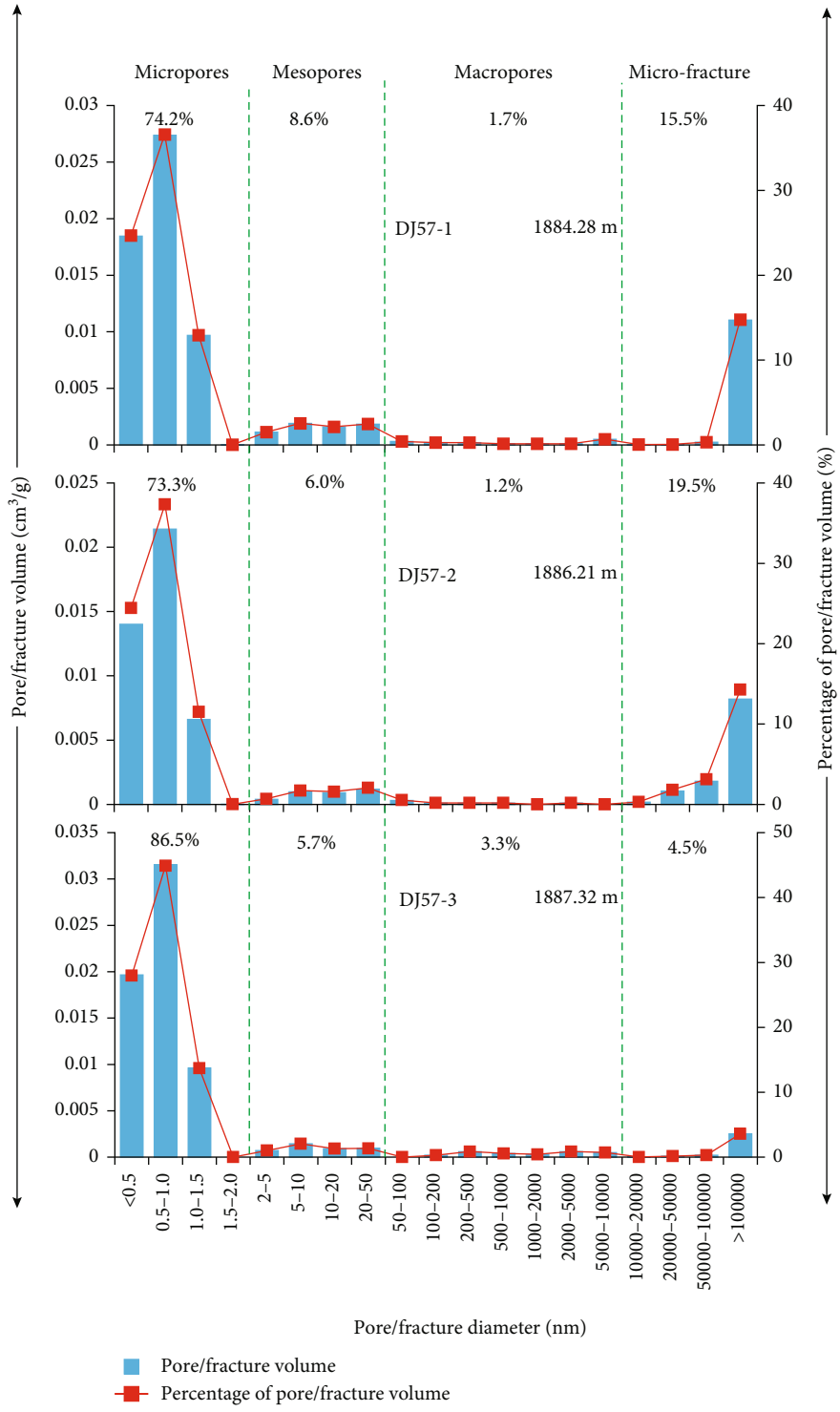

Figure 13: Volume distributions of micropores, mesopores, macropores, and microfractures and their percentages of volume in the Benxi coal samples analysed via LP-CO_2A, LT-N_2A, high-pressure MIP, and micro-CT.

followed by mesopores and microfractures, with average proportions of 6.78% and 13.14%, respectively; additionally, macropores are the least abundant, with an average proportion of 2.08%. The joint characterization results of pore size variation with SSA (Figure 14) reveal that the SSA distribution is mainly unimodal and that the peak SSA value is mainly concentrated in the pore size range of 0.3–1.5 nm. The SSAs of all the coal pores and fractures range from 145.0 to 209.3 m^2/g (mean 182.5 m^2/g). Among these components, the SSA of micropores makes the largest contribution, ranging from 143.7 to 207.4 m^2/g (mean 180.5 m^2/g). The mesopore contribution is the second highest, with an SSA ranging from 1.33 to 2.86 m^2/g (mean 2.03 m^2/g). The contributions of the macropores and microfractures are the

Table 3: Full-aperture pore structure characteristics of the coal samples.

Sample ID	PV (cm^3/g)					SSA (m^2/g)				
	Micropores	Mesopores	Macropores	Fractures	Total	Micropores	Mesopores	Macropores	Fractures	Total
DJ57-1	0.056	0.006	0.001	0.012	0.075	190.4	2.86	0.028	0.0004	193.3
DJ57-2	0.042	0.003	0.001	0.011	0.057	143.7	1.33	0.018	0.0009	145.0
DJ57-3	0.061	0.004	0.002	0.003	0.070	207.4	1.89	0.010	0.0002	209.3

Notes: PV = pore volume; SSA = specific surface area.

smallest. The SSA of the macropores is between 0.01 and 0.03 m^2/g. The SSA of the microfractures is between 0.0002 and 0.0009 m^2/g. The SSAs of pores and fissures at different scales are different (Figure 14 and Table 3). Among these components, micropores are the dominant pore SSA in the coal samples, accounting for 98.89% of the total pore SSA on average, and the SSA provided by mesopores, macropores, and microfractures can be ignored. Since the coal reservoirs of the Benxi Formation in the Daning–Jixian blocks are buried deep (>2000 m) and the associated vitrinite reflectance $R_o > 2.0\%$ indicates that the OM is in the overmature stage, with increasing coal rank, a large amount of gas is generated, resulting in abundant nanoscale pores in the OM and a high proportion of micropores overall. According to SEM observations of the coal samples from the study area, OM is widely distributed in the coal samples, and the presence of OM pores is one of the important reasons for the increase in porosity in the high-maturity stage of this coal. In addition, the contribution of microfractures to the total pore-fracture volume is approximately 13.1%. The main reasons include the following: (1) during the diagenetic evolution of the coal matrix or clay minerals in the Benxi Formation, many shrinkage-induced fractures formed due to geological processes such as mechanical compaction, dehydration, and degassing, which result in a large fracture volume; and (2) the Daning–Jixian block was tectonically located at the eastern margin of the Yishan Slope in the Ordos Basin and the southern end of the Jinxi Fault fold belt. This region has experienced intense periods of regional deformation and microstructural development. Affected by compressive stress, local high-point tensile fractures of folds are widely developed, and abundant secondary microfractures develop, resulting in a high volume proportion of microfractures [1, 2]. The PV and SSA of the coal samples are mainly attributed to micropore characteristics. Studies have shown that micropores provide many adsorption sites and occurrence spaces for CBM and are also important channels for the initial migration and diffusion of CBM after desorption; therefore, further study and analysis of the development and structural characteristics of CBM are necessary [13].

5.2. Contribution of the Pore-Fracture Structure to Permeability. Coal is a complex porous medium. According to the theory of dual-porosity structures, a porous medium includes both pores and fractures [53]. The pore-fracture system includes not only the occurrence space of CBM but also the migration channels of CBM. The characteristics of coal reservoirs, such as adsorbability, gas-bearing capacity, and permeability, are related to the development degree and structural characteristics of pores and fractures [53–55]. In this paper, a formula similar to that of Sinn et al. is used to calculate the deep coal reservoir permeability [56]. An ideal capillary bundle is assumed, and laminar flow through a cylindrical pipe is described by combining Darcy's law and the Hagen–Poiseuille equation to express permeability. Based on LT-N_2GA, the LP-CO_2GA method, and the high-pressure MIP method, the pore characteristics (PV, SSA, and pore diameter) of the coal samples can be quantitatively characterized; thus, the porosity corresponding to each pore can be calculated. Combined with the pore radius (r), the absolute permeability of a single pore can be further calculated (K_1) [56]:

$$K_1 = \frac{\varnothing_1 r_i^2}{8r^2}, \qquad K = \sum_{i=1}^{n} K_i, \tag{1}$$

where $\varnothing_i$ is the porosity corresponding to the ith pore and r_i is the radius of the ith pore. K_i is the absolute permeability of the ith pore. K is the calculated total pore permeability of the coal sample.

Based on micro-CT scanning and three-dimensional reconstruction technology, we quantitatively characterize the volume of microfractures and the total volume of coal samples after three-dimensional reconstruction, calculate the pore (fracture) clearance ($\varnothing$) corresponding to each microfracture, and then combine the microfracture width (ω) to further calculate the absolute permeability (K_1) of each microfracture [56]:

$$K_2 = \frac{\varnothing_i \omega_i^2}{12\tau^2}, \tag{2}$$

$$K = \sum_{i=1}^{n} K_i, \tag{3}$$

where $\varnothing_i$ is the microfracture degree of the ith microfracture and τ is the tortuosity of microfractures. In this study, $\tau = 10$ was used for calculation [56, 57], and K_i is the absolute permeability of the ith microfracture. K is the calculated total fracture permeability of the coal sample.

With LP-CO_2GA, LT-N_2GA, high-pressure MIP, and micro-CT scanning data, the pore and fracture volume of the coal samples can be quantitatively characterized (Table 3), and the pore (fracture) clearance corresponding to each pore and each microfracture can be calculated in combination with the pore radius and microfracture width.

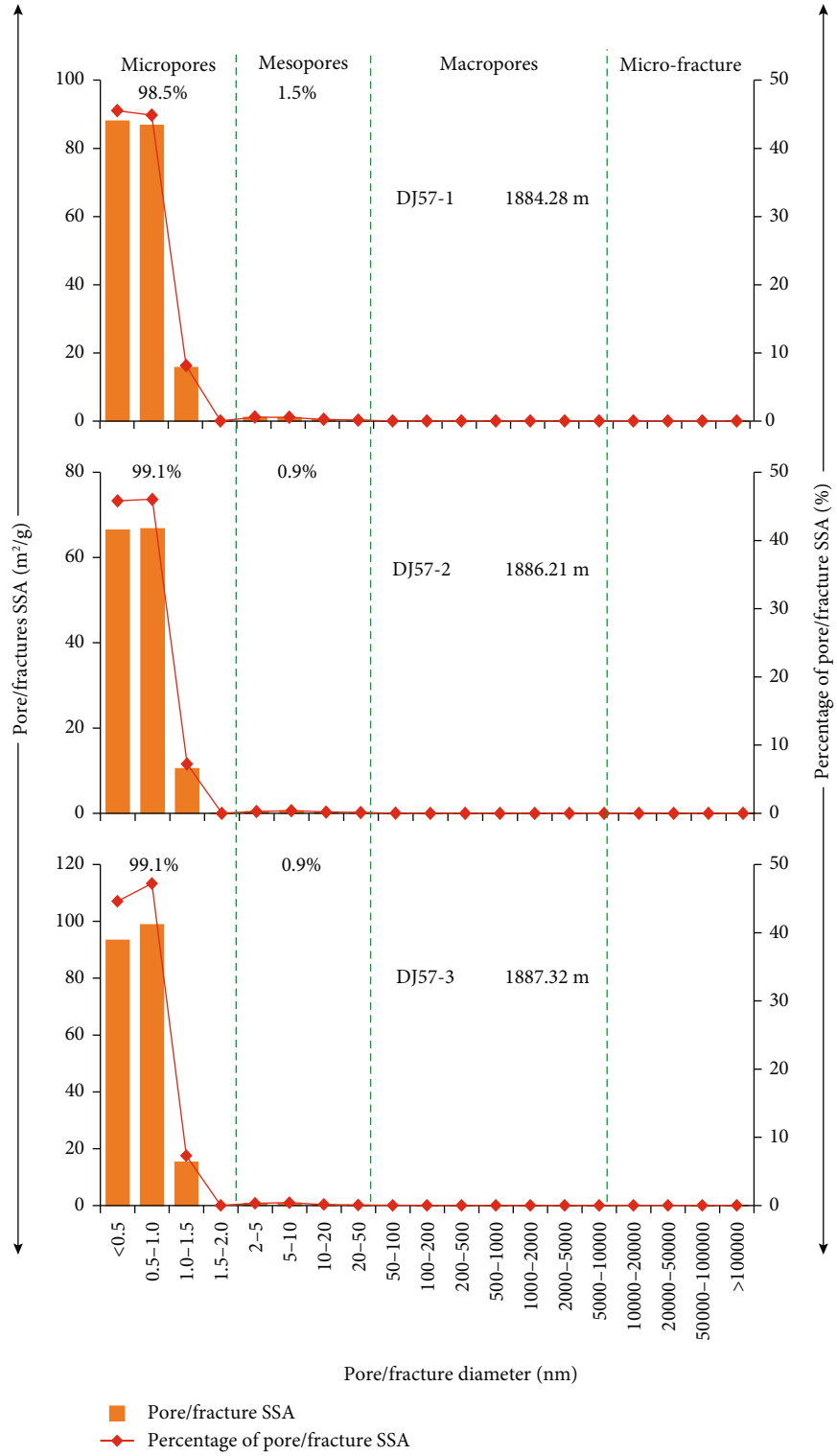

Figure 14: Micropores, mesopores, macropore, and microfracture SSA distributions and their SSA percentages in the Benxi coal analysed via LP-CO_2A, LT-N_2A, high-pressure MIP, and micro-CT.

The total permeability (sum of the pore permeability and fracture permeability) of the Benxi Formation ranges from 5.77 to 28.22 mD. There are three reasons for the slight difference between the calculated total permeability and the measured steady-state Farcke permeability (Figure 15). (1) When the steady-state Farcke permeability in a cylindrical sample (50 mm high with a diameter of 25 mm) is tested under a certain confining pressure (5 MPa), the microfractures may be partially or completely closed under the stress, which reduces the permeability of the coal samples. 2)

Although the tortuosity (τ) of microfractures is considered in the permeability calculation using the Hagen–Poiseuille equation (Equation (2)), the actual pore-fracture structure in coal samples is extremely complex, resulting in a relatively small measured permeability. (3) Through X-ray scanning and imaging, micro-CT technology can be used to identify not only connected microfractures but also isolated and closed microfractures [24, 47, 58]. Because these experimental procedures cannot be applied, the calculated fracture permeability is too high.

Figure 16 shows the contribution distribution of the pore (fracture) permeability to the calculated total permeability at the different pore segments. The permeability of the Benxi Formation coal samples is mainly controlled by microfractures with pore diameters > 100 μm, accounting for approximately 95% of the total permeability. The contribution of pores with diameters < 100 μm to the permeability of coal is relatively low, at only approximately 2% (Figure 16). The main reasons are as follows: the extent of microfractures > 100 μm is large, and more relatively independent pores and smaller microfractures can be connected spatially, thus forming a relatively developed microfracture network (Figures 10 and 11), which greatly improves the seepage capacity of coal samples [42, 43]. Although there are many large pores and small microfractures in the coal samples, these pores and microfractures are relatively spatially independent and have poor connectivity with each other (Figure 11); thus, they contribute little to the permeability of coal reservoirs.

5.3. Effect of the Pore-Fracture Structure on Gas Migration. The adsorption and desorption characteristics of CBM in nanoscale pores in microporous and fractured structures are studied. The microscale pores and connected pores in the structure are the main channels for CBM migration and play a decisive role in the flow migration of CBM and the permeability of coal reservoirs [55, 59]. In this paper, by combining the experimental methods of LP-CO_2GA, LT-N_2GA, high-pressure MIP, and micro-CT scanning, it was found that the pore-fracture structure of coal reservoirs is heterogeneous and spans multiple scale characteristics. The wide distribution of fractures from the nanoscale to the microscale results in the formation of a complex pore-fracture network (Figure 11). Therefore, based on a variety of pore characterization methods for the full-scale quantitative characterization of coal sample pores and fractures, there are obvious differences in the distributions of pores and fractures at different scales. The coal is mainly composed of 0.3–1.5 nm and >100 μm particles, in which the volume proportions of micropores (<2 nm), mesopores (2–50 nm), macropores (50 nm to 10 μm), and microfractures (>10 μm) are 78.00%, 6.78%, 2.08%, and 13.14%, respectively (Figure 13). This multiscale approach is highly important for the comprehensive evaluation of deep coal reservoir characteristics.

CBM mainly exists in the pore-fracture system of coal samples in adsorbed and free states. The adsorbed gas is mainly adsorbed on the surface of the coal matrix and clay mineral particles, and the free gas is mainly distributed in

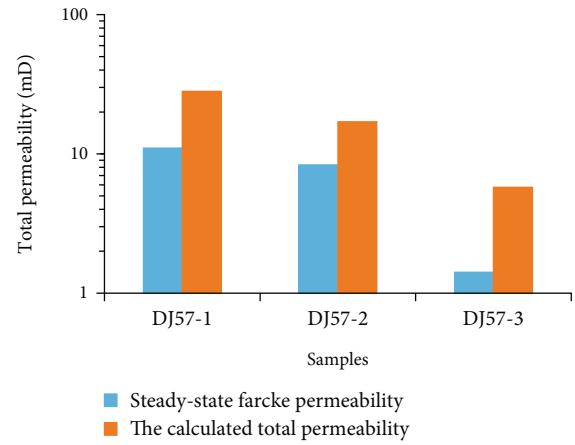

Figure 15: Comparison of the calculated total permeability and steady-state Farcke permeability.

the large pores and fractures of the coal. Yang et al. and Li et al. found that the deep coal seam in the eastern margin of the Ordos Basin is in a state of supersaturation with respect to gas content overall and that the proportion of free gas is 17-34%, with an average of approximately 20%, which is characterized by "high gas content, high gas saturation, and rich free gas" [60–63]. Tang et al. and Ma et al. studied the relationship between the pore structure at different scales and the gas content characteristics of deep coal reservoirs in the Daning–Jixian block. PV and SSA at different scales have different mechanisms of action on the CBM content in different phase states (Figure 17) [62, 64]. The adsorbed gas volume is closely related to the PV and SSA of the micropores, and the two variables have a strong linear relationship ($R^2 = 0.81$ and $R^2 = 0.79$, respectively; Figure 17). The results show that with the development of micropores, the adsorbed gas volume increases gradually, and micropores can provide many adsorption sites, which are conducive to gas adsorption and provide a place for the adsorption and occurrence of deep CBM. However, the free gas volume is closely related to the PV and SSA of microfractures, and these two variables are linearly positively correlated ($R^2 = 0.51$ and $R^2 = 0.63$, respectively; Figure 17), indicating that free gas mainly occurs in microfractures. The more developed the microfractures are, the more gas storage space is provided, and the greater the free gas volume is. The adsorbed gas in deep coal seams mainly occurs in micropores, which are mainly affected by the large adsorption SSA, while the free gas mainly occurs in microfractures, which are mainly affected by the gas volume.

According to the distribution characteristics of the Benxi Formation coal samples from the study area, the micropore PV of the coal samples ranges from 0.042 to 0.061 cm^3/g (mean 0.053 cm^3/g) (Table 3), which is slightly lower than that of Taiyuan Formation coal samples from the Qinshui Basin (0.046–0.062 cm^3/g) [15] and much greater than that of the shale of the Longmaxi Formation in the Sichuan Basin (mean 0.0104 cm^3/g) [64, 65]. The micropore SSA of the Benxi Formation coal samples ranges from 143.7 to 207.4 m^2/g (mean 180.5 m^2/g), which is similar to that of

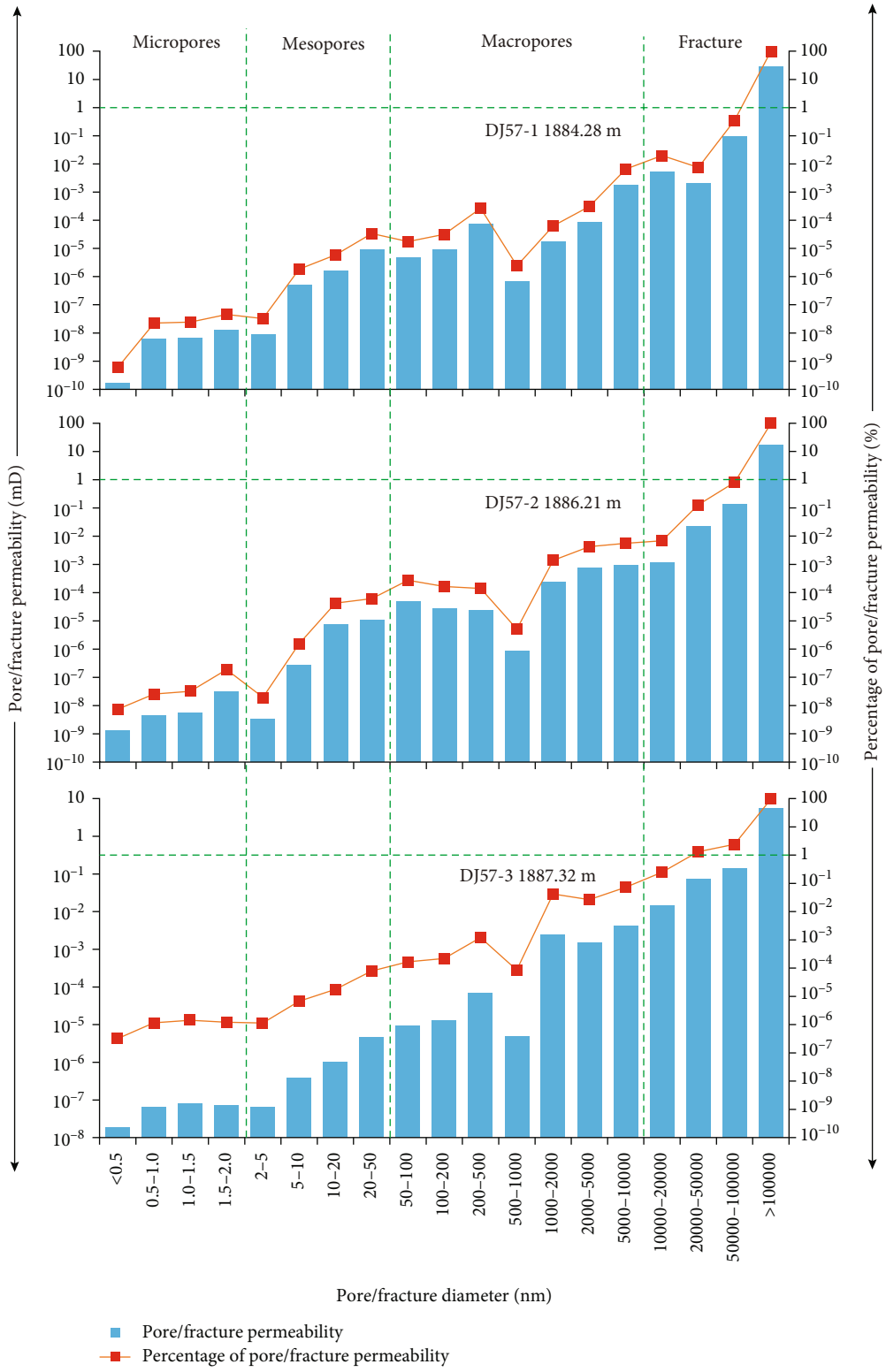

Figure 16: Distribution of the coal permeability contribution to the calculated total coal permeability in the various pore segments. DJ57-1 sample; DJ57-2 sample; DJ57-3 sample.

the coal samples from the Taiyuan Formation in the Qinshui Basin (139.6–209.129 cm^3/g) [15]. The Benxi Formation micropore SSA is dozens of times greater than that of the Longmaxi Formation shales (7.57–30.59 m^2/g) in the southeastern Sichuan Basin and the Shanxi Formation shales (0.655–11.42 m^2/g) in the eastern Ordos Basin [64, 65]. Because micropores can provide a large SSA, they can provide adsorption sites for methane molecular adsorption

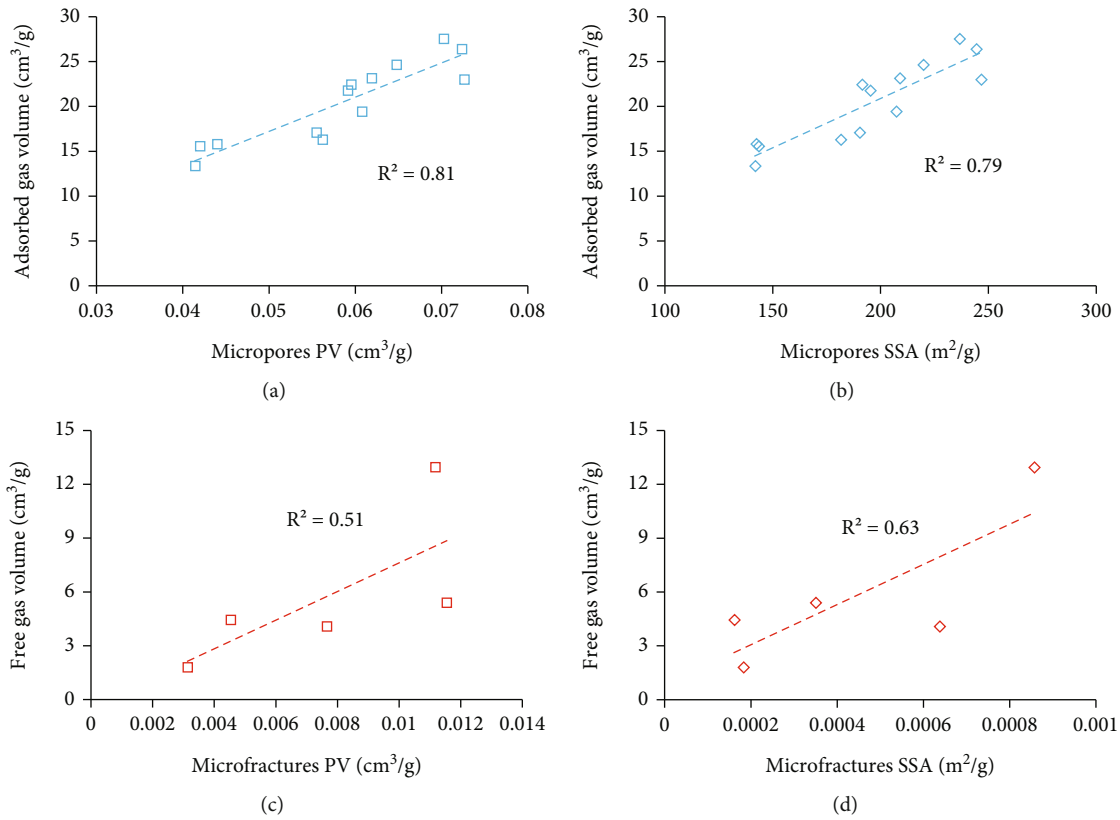

Figure 17: Relationships between the multiscale pore-fracture structure and gas content of the coal samples [60, 61]. (a) Micropore PV vs. adsorbed gas volume, (b) micropore SSA vs. adsorbed gas volume, (C) micropore PV vs. free gas volume, and (d) micropore SSA vs. free gas volume.

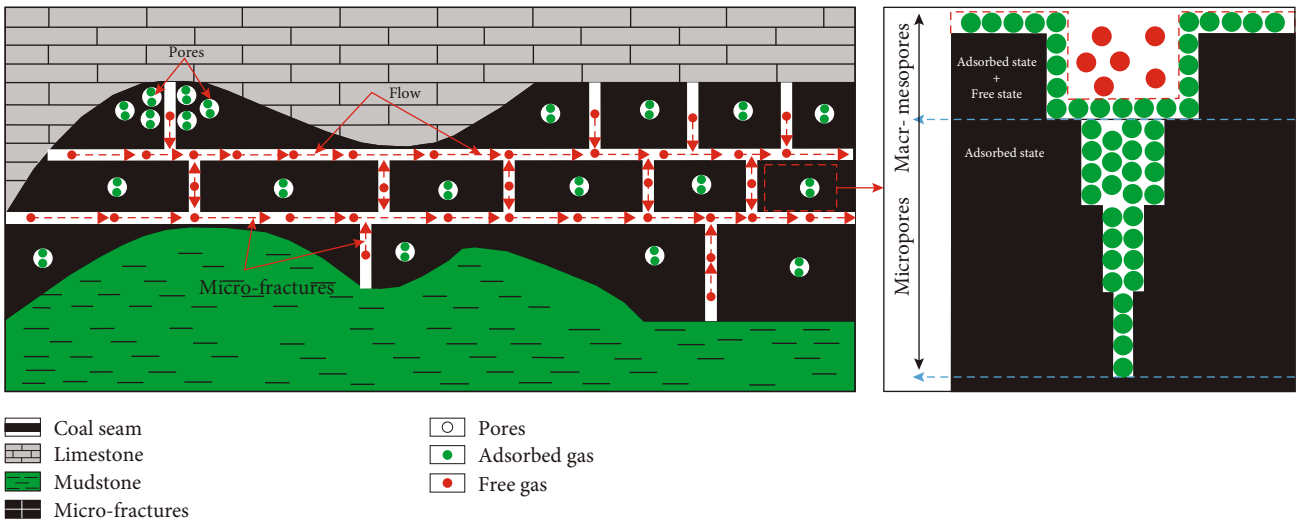

Figure 18: Schematic diagram of the CBM migration mechanism in the pores and fractures of coal.

and indirectly control the methane adsorption capacity in deep coal reservoirs. Moreover, micropores and microfractures, which are the main reservoir spaces available for free gas occurrence, have relatively low SSAs but play decisive roles in determining the permeability of coal reservoirs and CBM production [66, 67]. With the continuous desorption of gas in coal and the decrease in coal reservoir pressure, the amount of gas in pores and fractures in coal seams changes from increasing to decreasing, and multistage diffusion and penetration occur through interconnected nanoscale pores and microscale fractures [68]. Moreover, the form and scale of gas migration in pores and fractures at different scales are different, and interconnected pores and microfractures are effective channels for fluid transport (Figure 18). LP-CO_2GA, LT-N_2GA, high-pressure MIP, and micro-CT scanning are used to characterize the full-scale

pore-fracture structure of coal reservoirs. The advantageous pore distribution intervals determined by the respective experiments are utilized to quantitatively characterize the micropores, mesopores, macropores, and microfractures. Among them, the development characteristics of micropores and microfractures control the adsorption capacity and development potential of deep CBM, respectively. Research on the development characteristics of nanoscale pores and microscale fractures plays a decisive role in the enrichment and exploitation potential of deep CBM, and further research on the migration mechanism, scale, and controlling factors of deep CBM is needed.

6. Conclusions

The results of this study on the characteristics of pore structure in a deep coal reservoir and its influence on CBM occurrence, with a case study of the Daning–Jixian block, support the following conclusions:

(1) The coal samples from the Benxi Formation are mainly composed of OM pores, inorganic pores, and microfractures. The OM pores have various shapes, mainly round, elliptical, and wedge-shaped. The inorganic pores can be divided into intraparticle and interparticle pores. The diameters of the intraparticle pores are small, between 20 and 50 nm, while the diameters of the interparticle pores are larger, generally greater than 300 nm. The microfractures are mainly distributed within the margins of the coal matrix and inside the clay minerals and are elongated or zigzag-shaped

(2) According to the full-scale quantitative characterization of the pore and fracture volume distributions with respect to pore size, the PSD is mainly U-shaped, exhibiting a bimodal state of micropores and microfractures, which are mainly concentrated in the ranges of 0.3–1.5 nm and >100 μm, respectively. The pore-fracture volume is dominated by micropores (average volume proportion of 78.0%), followed by mesopores and microfractures (average volume proportions of 6.8% and 13.1%, respectively). Macropores were the least common (mean 2.1%)

(3) The microfractures are interconnected in three-dimensional space, forming a network structure with strong connectivity. The permeability is mainly contributed by microfractures with pore diameters > 100 μm, accounting for approximately 95% of the total permeability. These findings indicate that microfractures are the main channels for deep CBM migration and play a decisive role in the flow of deep CBM

(4) By combining experimental methods such as LP-CO_2GA, LT-N_2GA, high-pressure MIP, and micro-CT scanning, we determine that the pore structure of deep coal reservoirs is heterogeneous and spans multiple scales. The development characteristics of nanoscale pores and micrometre fractures control the enrichment capacity and development potential of deep CBM, respectively

Data Availability

The data used to support the findings of this study are included within the article.

Conflicts of Interest

The authors declare that there is no conflict of interest regarding the publication of this paper.

Funding

This research was jointly supported by Grant No. 2022KT1401 and Grant No. 2021DJ2302.

Acknowledgments

We thank PetroChina Coalbed Methane Company, Ltd., for collecting the samples.

References

[1] F. Xu, C. Wang, X. Xiong et al., "Deep(layer) coalbed methane reservoir forming modes and key tech-nical countermeasures: taking the eastern margin of Ordos Basin as an example," *China Offshore Oil and Gas*, vol. 34, no. 4, pp. 30–42, 2022.

[2] T. Wang, Z. Deng, H. Hu et al., "Pore structure of deep coal of different ranks and its effect on coalbed methane adsorption," *International Journal of Hydrogen Energy*, vol. 59, pp. 144–158, 2024.

[3] F. Xu, Z. Xiao, D. Chen et al., "Current status and development direction of coalbed methane exploration technology in China," *Coal Science and Technology*, vol. 47, no. 10, pp. 205–215, 2019.

[4] Q. Wei, X. Li, J. Zhang et al., "Full-size pore structure characterization of deep-buried coals and its impact on methane adsorption capacity: a case study of the Shihezi Formation coals from the Panji Deep Area in Huainan coalfield, southern North China," *Journal of Petroleum Science and Engineering*, vol. 173, pp. 975–989, 2019.

[5] H. Gan, S. P. Nandi, and J. P. L. Walker, "Nature of the porosity in American coals," *Fuel*, vol. 51, no. 4, pp. 272–277, 1972.

[6] A. J. Martin, S. T. Solomon, and D. J. Hartmann, "Characterization of petrophysical flow units in carbonate reservoirs," *AAPG Bulletin*, vol. 81, no. 5, pp. 734–759, 1995.

[7] R. G. Loucks, R. M. Reed, S. C. Ruppel, and U. Hammes, "Spectrum of pore types and networks in mudrocks and a descriptive classification for matrix-related mudrock pores," *AAPG Bulletin*, vol. 96, no. 6, pp. 1071–1098, 2012.

[8] K. S. W. Sing, D. V. Everett, R. A. W. Haul et al., "Reporting physisorption data for gas/solid systems with special reference to the determination of surface area and porosity (recommendations 1984)," *Pure and Applied Chemistry*, vol. 57, no. 4, pp. 603–619, 1985.

[9] Q. Gou, S. Xu, F. Hao et al., "Full-scale pores and microfractures characterization using FE-SEM, gas adsorption, nano-CT and micro-CT: a case study of the Silurian Longmaxi Formation shale in the Fuling area, Sichuan Basin, China," *Fuel*, vol. 253, pp. 167–179, 2019.

[10] X. Xu, Z. Meng, and Y. Wang, "Experimental comparisons of multiscale pore structures between primary and disturbed coals and their effects on adsorption and seepage of coalbed

methane," *Journal of Petroleum Science and Engineering*, vol. 174, pp. 704–715, 2019.

[11] P. Mou, J. Pan, Q. Niu, Z. Wang, Y. Li, and D. Song, "Coal pores: methods, types, and characteristics," *Energy & Fuels*, vol. 35, no. 9, pp. 7467–7484, 2021.

[12] J. Yan, Z. Meng, K. Zhang, H. Yao, and H. Hao, "Pore distribution characteristics of various rank coals matrix and their influences on gas adsorption," *Journal of Petroleum Science and Engineering*, vol. 189, article 107401, 2020.

[13] D. Song, X. Ji, Y. Li, H. Zhao, B. Song, and K. He, "Heterogeneous development of micropores in medium-high rank coal and its relationship with adsorption capacity," *International Journal of Coal Geology*, vol. 226, article 103497, 2020.

[14] T. Wang, F. Tian, Z. Deng, H. Hu, and Z. Xie, "The pore structure of marine to continental transitional shales in the Permian Shanxi Formation on the east margin of the Ordos Basin, China," *Geofluids*, vol. 2022, Article ID 5601862, 21 pages, 2022.

[15] T. Wang, F. Tian, Z. Deng, and H. Hu, "The characteristic development of micropores in deep coal and its relationship with adsorption capacity on the eastern margin of the Ordos Basin, China," *Minerals*, vol. 13, no. 3, p. 302, 2023.

[16] J. Sun, X. Zhao, and S. Sang, "Development characteristics, origins and significance of coal seam fractures under optical microscope: taking coal seam $3^{\#}$ in southern Qinshui Basin as an example," *Fault-Block Oil & Gas Field*, vol. 23, no. 6, pp. 738–744, 2016.

[17] S. Zhu, Z. Du, C. Li et al., "Effects of numerical dispersion on pressure diffusion in CBM reservoirs," *Fuel*, vol. 251, pp. 534–542, 2019.

[18] P. Wang, P. Lv, Z. Jiang et al., "Comparison of organic matter pores of marine and continental facies shale in China: based on focused ion beam helium ion microscopy (FIB-HIM)," *Petroleum Geology Experiment*, vol. 40, no. 5, pp. 739–748, 2018.

[19] T. Wang, Z. Deng, H. Hu et al., "Pore structure and fractal characteristics of transitional shales with different lithofacies from the eastern margin of the Ordos Basin," *Energy Science & Engineering*, vol. 11, no. 11, pp. 3979–4000, 2023.

[20] S. Zhou, D. Liu, Y. Cai, Y. Yao, and Z. Li, "3D characterization and quantitative evaluation of pore-fracture networks of two Chinese coals using FIB-SEM tomography," *International Journal of Coal Geology*, vol. 174, pp. 41–54, 2017.

[21] G. Okolo, R. Everson, H. Neomagus, M. Roberts, and R. Sakurovs, "Comparing the porosity and surface areas of coal as measured by gas adsorption, mercury intrusion and SAXS techniques," *Fuel*, vol. 141, pp. 293–304, 2015.

[22] M. Cheng, X. Fu, and J. Kang, "Compressibility of different pore and fracture structures and its relationship with heterogeneity and minerals in low-rank coal reservoirs: an experimental study based on nuclear magnetic resonance and micro-CT," *Energy & Fuels*, vol. 34, no. 9, pp. 10894–10903, 2020.

[23] X. Shi, J. Pan, Q. Hou et al., "Micrometer-scale fractures in coal related to coal rank based on micro-CT scanning and fractal theory," *Fuel*, vol. 212, pp. 162–172, 2018.

[24] Y. Yao and D. Liu, "Comparison of low-field NMR and mercury intrusion porosimetry in characterizing pore size distributions of coals," *Fuel*, vol. 95, pp. 152–158, 2012.

[25] Y. Zhao, Y. Sun, S. Liu, K. Wang, and Y. Jiang, "Pore structure characterization of coal by NMR cryoporometry," *Fuel*, vol. 190, pp. 359–369, 2017.

[26] A. Radlinski, M. Mastalerz, A. Hinde et al., "Application of SAXS and SANS in evaluation of porosity, pore size distribution and surface area of coal," *International Journal of Coal Geology*, vol. 59, no. 3-4, pp. 245–271, 2004.

[27] D. Li, Y. Bao, Y. Wang, C. An, and J. Chang, "Multiple-experimental investigation on the physicochemical structures alternation during coal biogasification," *Fuel*, vol. 339, article 127433, 2023.

[28] W. Li, H. Yao, H. Liu, Z. Kang, X. Song, and Z. Feng, "Advanced characterization of three-dimensional pores in coals with different coal-body structure by micro-CT," *Journal of China Coal Society*, vol. 39, no. 6, pp. 1127–1132, 2014.

[29] X. Jia, H. Niu, H. Liu, W. Li, and H. Yao, "Quantitative characterization of pore fissures for different coal structures based on μCT," *Safety in Coal Mines*, vol. 49, no. 11, pp. 24–28, 2018.

[30] C. Li, B. Jiang, W. Ju, G. Cheng, and Y. Song, "Characteristics of tectonic deformation in the Daning-Jixian region, eastern Ordos Basin: implications for the exploration and development of coalbed methane," *Energy Exploration & Exploitation*, vol. 37, no. 3, pp. 907–921, 2019.

[31] S. Li, C. Wang, H. Wang et al., "Reservoir forming characteristics and favorable area evaluation of deep coalbed methane in Daning-Jixian block," *Coal Geology & Exploration*, vol. 50, no. 9, pp. 1–9, 2022.

[32] S. Brunauer, P. H. Emmett, and E. Teller, "Adsorption of gases in multimolecular layers," *Journal of the American Chemical Society*, vol. 60, no. 2, pp. 309–319, 1938.

[33] E. P. Barrett, L. G. Joyner, and P. P. Halenda, "The determination of pore volume and area distributions in porous substances. I. Computations from nitrogen isotherms," *Journal of the American Chemical Society*, vol. 73, no. 1, pp. 373–380, 1951.

[34] C. R. Clarkson, N. Solano, R. M. Bustin et al., "Pore structure characterization of North American shale gas reservoirs; using usans/sans, gas adsorption, and mercury intrusion," *Fuel*, vol. 103, no. 1, pp. 606–616, 2013.

[35] D. J. K. Ross and B. R. Marc, "The importance of shale composition and pore structure upon gas storage potential of shale gas reservoirs," *Marine and Petroleum Geology*, vol. 26, no. 6, pp. 916–927, 2009.

[36] R. Evans, U. M. B. Marconi, and P. Tarazona, "Capillary condensation and adsorption in cylindrical and slit-like pores," *Journal of the Chemical Society*, vol. 82, no. 10, pp. 1763–1787, 1986.

[37] M. E. Curtis, C. H. Sondergeld, R. J. Ambrose, and C. S. Rai, "Microstructural investigation of gas shales in two and three dimensions using nanometer–scale resolution imaging," *AAPG Bulletin*, vol. 96, no. 4, pp. 665–677, 2012.

[38] E. Washburn, "The dynamics of capillary flow," *Physical Review Journals Archive*, vol. 17, no. 3, pp. 273–283, 1921.

[39] J. Rouquerol, D. Avnir, C. W. Fairbridge et al., "Recommendations for the characterization of porous solids (technical report)," *Pure and Applied Chemistry*, vol. 66, no. 8, pp. 1739–1758, 1994.

[40] S. Chen, S. Tao, D. Tang et al., "Pore structure characterization of different rank coals using $_{N2and}$ CO2 adsorption and its effect on CH4 adsorption capacity: a case in Panguan Syncline, Western Guizhou, China," *Energy & Fuels*, vol. 31, no. 6, pp. 6034–6044, 2017.

[41] B. Wang, Y. Qin, J. Shen, J. Shen, Q. Zhang, and G. Wang, "Pore structure characteristics of low- and medium-rank coals and their differential adsorption and desorption effects," *Journal of Petroleum Science and Engineering*, vol. 165, pp. 1–12, 2018.

[42] C. O. Karacan and G. D. Mitchell, "Behavior and effect of different coal microlithotypes during gas transport for carbon dioxide sequestration into coal seams," *International Journal of Coal Geology*, vol. 53, no. 4, pp. 201–217, 2003.

[43] F. J. Simons and R. Swennen, "Quantitative characterization of coal by means of microfocal X-ray computed microtomography (CMT) and color image analysis (CIA)," *International Journal of Coal Geology*, vol. 34, no. 1–2, pp. 69–88, 1997.

[44] J. P. Mathews, Q. P. Campbell, H. Xu, and P. Halleck, "A review of the application of X-ray computed tomography to the study of coal," *Fuel*, vol. 209, pp. 10–24, 2017.

[45] Y. Yao, D. Liu, D. Che, D. Tang, S. Tang, and W. Huang, "Non-destructive characterization of coal samples from China using microfocus X-ray computed tomography," *International Journal of Coal Geology*, vol. 80, no. 2, pp. 113–123, 2009.

[46] J. Liu, X. Jiang, X. Huang, and S. Wu, "Morphological characterization of superfine pulverized coal particles," *Energy & Fuels*, vol. 24, no. 5, pp. 844–855, 2010.

[47] H. Fang, S. Sang, S. Liu, and Y. Du, "Methodology of three-dimensional visualization and quantitative characterization of nanopores in coal by using FIB-SEM and its application with anthracite in Qinshui basin," *Journal of Petroleum Science and Engineering*, vol. 182, article 106285, 2019.

[48] T. Cao, Z. Song, H. Luo, Y. Zhou, and S. Wang, "Pore system characteristics of the Permian transitional shale reservoir in the lower Yangtze region, China," *Journal of Natural Gas Science and Engineering*, vol. 1, no. 5, pp. 383–395, 2016.

[49] S. Barnard, R. Wirth, A. Schreiber, H. M. Schulz, and B. Horsfield, "Formation of nanoporous pyrobitumen residues during maturation of the Barnett Shale (Forth Worth basin)," *International Journal of Coal Geology*, vol. 103, pp. 3–11, 2012.

[50] M. M. Labani, R. Rezaee, A. Saeedi, and A. A. Hinai, "Evaluation of pore size spectrum of gas shale reservoirs using low pressure nitrogen adsorption, gas expansion and mercury porosimetry: a case study from the Perth and Canning Basins, Western Australia," *Journal of Petroleum Science and Engineering*, vol. 112, pp. 7–16, 2013.

[51] G. Wang, Y. Ju, Z. Yan, and Q. Li, "Pore structure characteristics of coalbearing shale using fluid invasion methods: a case study in the Huainan–Huaibei coalfield in China," *Marine and Petroleum Geology*, vol. 62, pp. 1–13, 2015.

[52] Y. Zhao, S. Liu, D. Elsworth, Y. Jiang, and J. Zhu, "Pore structure characterization of coal by synchrotron small-angle X-ray scattering and transmission electron microscopy," *Energy & Fuels*, vol. 28, no. 6, pp. 3704–3711, 2014.

[53] Y. Zhao, T. Liu, N. N. Danesh, Y. Sun, S. Liu, and Y. Wang, "Quantification of pore modification in coals due to pulverization using synchrotron small angle X-ray scattering," *Journal of Natural Gas Science and Engineering*, vol. 84, article 103669, 2020.

[54] Z. Pan and L. D. Connell, "Modelling permeability for coal reservoirs: a review of analytical models and testing data," *International Journal of Coal Geology*, vol. 92, pp. 1–44, 2012.

[55] M. Pillalamarry, S. Harpalani, and S. Liu, "Gas diffusion behavior of coal and its impact on production from coalbed methane reservoirs," *International Journal of Coal Geology*, vol. 86, no. 4, pp. 342–348, 2011.

[56] C. J. A. Sinn, J. Klaver, R. Fink et al., "Using BIB-SEM imaging for permeability prediction in heterogeneous shales," *Geofluids*, vol. 2017, Article ID 4709064, 19 pages, 2017.

[57] T. Philipp, A. Amann-Hildenbrand, B. Laurich, G. Desbois, R. Littke, and J. L. Urai, "The effect of microstructural heterogeneity on pore size distribution and permeability in Opalinus Clay (Mont Terri, Switzerland): insights from an integrated study of laboratory fluid flow and pore morphology from BIB-SEM images," *Geological Society, London, Special Publications*, vol. 454, no. 1, pp. 85–106, 2017.

[58] S. Liu, S. Sang, G. Wang et al., "FIB-SEM and X-ray CT characterization of interconnected pores in high-rank coal formed from regional metamorphism," *Journal of Petroleum Science and Engineering*, vol. 148, pp. 21–31, 2017.

[59] P. D. Gamson, B. B. Beamish, and D. P. Johnson, "Coal microstructure and micropermeability and their effects on natural gas recovery," *Fuel*, vol. 72, no. 1, pp. 87–99, 1993.

[60] J. Yang, P. Feng, S. Tang et al., "Quantitative prediction of deep coalbed methane Content in Daning-Jixian Block, Ordos Basin, China," *Acta Petrolei Sinica*, vol. 11, no. 11, pp. 1891–3093, 2023.

[61] Y. Li, S. Gao, P. Wu et al., "Evaluation and correction of prediction model for free gas content in deep coalbed methane: a case study of deep coal seams in the eastern margin of Ordos Basin," *Acta Petrolei Sinica*, vol. 44, no. 11, pp. 1892–1902, 2023.

[62] S. Tang, D. Tang, J. Yang et al., "Pore structure characteristics and gas storage potential of deep coal reservoirs in Daning-Jixian block of Ordos Basin," *Acta Petrolei Sinica*, vol. 44, no. 11, pp. 1854–1866, 2023.

[63] Y. Bao, Z. Li, J. Meng, X. Chen, and X. Liu, "Reformation of coal reservoirs by microorganisms and its significance in CBM exploitation," *Fuel*, vol. 360, article 130642, 2024.

[64] Y. Ma, Z. Pan, N. Zhong et al., "Experimental study of anisotropic gas permeability and its relationship with fracture structure of Longmaxi shales, Sichuan Basin, China," *Fuel*, vol. 180, pp. 106–115, 2016.

[65] Z. Li, I. A. Oyediran, R. Huang et al., "Study on pore structure characteristics of marine and continental shale in China," *Journal of Natural Gas Science and Engineering*, vol. 33, pp. 143–152, 2016.

[66] S. Zhu, X. Peng, Z. You, C. Li, and P. Deng, "The effects of cross-formational water flow on production in coal seam gas reservoir: a case study of Qinshui Basin in China," *Journal of Petroleum Science and Engineering*, vol. 194, article 107516, 2020.

[67] Z. Zhang, Y. Qin, G. Wang et al., "Evaluation of coal body structures and their distributions by geophysical logging methods: case study in the Laochang block, eastern Yunnan, China," *Natural Resources Research*, vol. 30, no. 3, pp. 2225–2239, 2021.

[68] Z. Wang, S. Hurter, Z. You, V. Honari, Y. Sun, and S. Zhang, "Influences of negative pressure on air-leakage of coalseam gas extraction: laboratory and CFD-DEM simulations," *Journal of Petroleum Science and Engineering*, vol. 196, article 107731, 2021.